Lanthanum-based Double Perovskite Nanoscale Motifs as Support Media for the Methanol Oxidation Reaction

Scott C. McGuire[1], Christopher Koenigsmann[2], Chun Chieh Chou[1], Xiao Tong[3], and Stanislaus S. Wong[1,*]

Email: stanislaus.wong@stonybrook.edu

[1]Department of Chemistry, State University of New York at Stony Brook, Stony Brook, NY 11794-3400

[2]Department of Chemistry, Fordham University, Bronx, NY 10458

[3]Center for Functional Nanomaterials, Building 735, Brookhaven National Laboratory, Upton, NY 11973

Abstract. We have not only analyzed the performance of perovskite oxides as support media for the methanol oxidation reaction (MOR) but also examined the impact and significance of various reaction parameters on their synthesis. Specifically, we have generated (a) La_2NiMnO_6, $LaMnO_3$, and $LaNiO_3$ nanocubes with average sizes of ~200 nm, in addition to a series of La_2NiMnO_6 (b) nanocubes possessing average sizes of ~70 and 400 nm and (c) anisotropic nanorods characterized by average diameters of 40-50 nm. All of these samples, when used as supports for Pt nanoparticles, exhibited activities which were at least twice that measured for Pt/C. We have investigated and correlated the effect of varying perovskite (i) composition, (ii) size, and (iii) morphology upon the measured MOR activity. (i) The Ni-containing perovskites yielded generally higher performance metrics than that of $LaMnO_3$ alone, suggesting that the presence of Ni is favorable for MOR, a finding supported by a shift in the Pt *d*-band in XPS. (ii) MOR activity is enhanced as the perovskite size increases in magnitude, suggesting that a growth in the perovskite particle size enables favorable, synergistic metal-support interactions. (iii) A comparison of the nanorods and nanocubes of a similar diameter implied that the one-dimensional morphology achieved a greater activity, a finding which can be attributed not only to the anisotropic structure but also to a desirable surface structure. Overall, these data yield key insights into the tuning of metal-support interactions via rational control over the composition, size, and morphology of the underlying catalyst support.

Introduction

Precious metal electrocatalysts for both small organic molecule (SOM) oxidation and oxygen reduction are typically deposited onto an underlying support, which is intended to increase precious metal utilization. Support materials not only provide a substrate for the catalyst particles but also simultaneously decrease catalyst particle aggregation and slow ripening processes during electrochemical operation.[1] As a class of materials, metal oxides, such as but not limited to TiO_2,[2-6] RuO_2,[7-8] and WO_3,[9-12] represent viable alternatives to standard carbon black as supports, due to their increased chemical and electrochemical stability at high potential in acidic media and favorable, synergistic interactions with the coated electrocatalysts.[13] More importantly, the surfaces of metal oxides can facilitate the oxidation and removal of partially oxidized intermediates, such as CO from Pt catalysts, by providing for oxide and hydroxide species at the catalytic interface and facilitating the transport of protons and hydroxide in aqueous conditions.[14] Metal oxides can act as a co-catalyst through beneficial interactions with the overlying metal; these are defined in the context of strong metal-support interactions (SMSI). The SMSI effect can be manifested through either charge transfer between the support and catalyst, a change in lattice parameter of the catalyst itself, or a combination of both factors.[15-17]

To take this idea one step further, we have examined complex metal oxides, such as perovskites, as catalyst supports. Perovskite metal oxides possess the general formula of ABO_3, wherein A represents a larger cation and B is a smaller cation. By analogy with binary metal oxides, perovskites can be electronically conductive, maintain good stability, and possess very good proton transport properties; moreover, their surfaces are protonated under acidic conditions, thereby rendering them as excellent candidates for support materials for MOR under highly

acidic environments.[18-19] Furthermore, the chemical composition of ternary ABO_3 materials can be tuned so as to optimize their performance.

In general, altering the chemical identity of both the A and B site metals within perovskites characterized by the general formula of ABO_3 can impact upon their observed catalytic activity. In particular, the A site metal has been previously shown to influence several important properties of perovskites, including their electroconductivity and surface adsorption properties, which are relevant to predicting their electrocatalytic performance.[19-20] For example, catalytic performance was noted to be highly dependent upon the identity of the metal in the A site within $AMnO_3$, with the measured MOR activity increasing as follows: A = Dy < Sm < Pr < Y < La.[21] In addition, changing the B site metal can also impact upon the observed MOR activity. Specifically, the presence of Mn was shown to yield improved activities as compared with Co and Fe, when incorporated as the B site of $LaBO_3$.[22] Moreover, the oxidation states of the constituent metals are also significant determinants of electrocatalytic activity, because the sum of the overall charges associated with the metal cations and oxygen anions may be non-zero, such that either an oxygen deficiency or a corresponding oxygen excess may arise.[23]

Perovskites exhibit multiple complementary functionalities as both active catalysts and support media. For instance, one study investigated a series of rare earth perovskites, including $La_{1-x}Mn_{1-y}O_{3-\delta}$, $La_{1-x}Fe_{1-y}O_{3-\delta}$, $La_{1-x}Cr_{1-y}O_{3-\delta}$, $La_{1-x}Ni_{1-y}O_{3-\delta}$, $(La, Sr)_{1-x}Fe_{1-y}O_{3-\delta}$, and $La_{1-x}(Fe, Ca)_{1-y}O_{3-\delta}$ ($x > 0.0$, $y < 0.2$), in terms of their applicability as electrocatalysts for direct methanol fuel cells.[24] Out of these perovskites, both $La_{1-x}Mn_{1-y}O_{3-\delta}$ and $La_{1-x}Fe_{1-y}O_{3-\delta}$ evinced good stability; furthermore, the latter species yielded comparable electrocatalytic activity to that of Pt/C. As a second example, $SrFeO_3$ nanoparticles, when used as supports for Pt nanoparticles, achieved specific activities for MOR which were nearly five times higher than those obtained for

Pt nanoparticles.[25] Moreover, these $SrFeO_3$-based catalysts gave rise to improved stabilities, attributable to their higher tolerance to CO poisoning. As a third instance, $LaNiO_3$ nanocubes are also known as viable catalyst supports.[26] Specifically, Pt/$LaNiO_3$ nanocube catalysts yielded not only a negative onset shift of 0.1 and 0.23 V but also superior stability as compared with Pt/C and unsupported Pt, respectively. Moreover, $LaNiO_3$-supported catalysts achieved 3-fold greater mass activities and 2-fold higher specific activities in acidic media as compared with Pt/C. Overall, when used as supports, perovskite metal oxides evinced increases in both activity and stability, especially as compared with either bare or carbon-supported Pt catalysts.

While prior studies have demonstrated that the specific chemical composition of the support material yielded a considerable impact on MOR activity, the size and shape of the underlying metal oxide support are also important factors. For example, our group initially showed that the *size* of the support materials played a significant role in terms of the measured activity with smaller particles yielding higher activity.[27] Specifically, we found that for both $SrTiO_3$ (STO)/Pt and $SrRuO_3$ (SRO)/Pt catalysts probed at 0.55 V vs. RHE, the smaller particles (i.e., ~40 nm) gave rise to appreciably greater activities as compared with the larger particles (>100 nm), with all other parameters adequately controlled and taken into consideration. This size-dependent difference in activity was likely caused by a change in surface area, with smaller particles evincing larger active exposed surface areas.

To reinforce the importance of *shape*, in a complementary study, we analyzed the structure-dependent MOR activity of SRO by comparing the activity of faceted octahedra versus that of rounded nanoparticles, possessing similar sizes.[28] The well-defined faceted octahedra achieved mass activities that were nearly four times greater than that of rounded particles. This

increase in activity was again attributed to the higher exposed surface area of the octahedra, which was ~4 times greater than that of the rounded nanoparticles.

Other groups have also reported on the crucial role of morphology in dictating MOR performance. As an example, studies have compared the activities of MnO_2 urchin-like structures composed of constituent nanorods versus that of MnO_2 microcubes within the context of $Pt/MnO_2/C$ composites.[29] The urchin-like nanostructures achieved both a higher activity and an improved stability for MOR as compared with that of the corresponding microcubes. To account for this finding, in addition to surface area considerations, the greater activity of the nanorods could be attributed to their tendency to provide for active interfaces between the Pt, the metal oxide, and the surrounding electrolyte, so as to enable better adsorption of oxidizing species, which could favorably oxidize poisoning species and thereby increase the observed stability.

Nevertheless, whereas conventional ABO_3 perovskites have certainly shown promise as catalyst support materials for MOR, little to no work has yet to be reported on the use of double perovskites (with the structure of $A_2BB'O_6$) as supports. The majority of work concerning double perovskites has focused on their structural and magnetic properties,[30-33] as well as their potential applicability as catalysts for the oxygen evolution and oxygen reduction reactions (OER/ORR).[34-38] By analogy with single perovskites, double perovskites display excellent chemical stability, are electronically conductive, and should possess the ability to form hydroxyl groups on their external surface. Moreover, the $A_2BB'O_6$ formula allows for the potential for even more complex compositional tuning (including the formation of mixed valence states), which can be beneficial in developing a novel class of state-of-the-art supports. Additionally, double perovskites can maintain higher amounts of oxygen defects than their single perovskite analogues,[39] a finding which can potentially increase their activity. One such example, which is

suggestive of the promising potential of double perovskites in yielding higher MOR performance, involves the use of $LaMn_{1-x}Ni_xO_3$ perovskites for the catalytic oxidation of ethanol. In effect, $LaMn_{1-x}Ni_xO_3$ gave rise to increased activities as compared with either $LaMnO_3$ or $LaNiO_3$ alone,[40] a finding attributable to the partial substitution of Mn with Ni within $LaMnO_3$ and associated with the presence of favorable Ni-O-Mn interactions.

Although considerable work has been performed on single perovskites in the prior literature, there has been comparably less effort devoted to exploring double perovskites as catalyst supports for MOR. As such, herein, we examine the influence of morphology, particle size, and composition of double perovskite supports on the resulting catalytic activity toward MOR. In addition, we also compare the MOR performance of double perovskites to single perovskites to reinforce the intrinsic catalytic benefits of the double perovskite structure. Specifically, we have synthesized $LaMnO_3$ (LMO), $LaNiO_3$ (LNO), and La_2NiMnO_6 (LNMO), possessing discrete morphologies. The double perovskite structure offers several advantages that can facilitate their performance toward small organic molecule oxidation. For example, the precise combination of metals within the double perovskite will promote a higher mixture of valence states as compared with the single perovskite analogues alone,[41-43] which can be utilized to rationally tune for enhanced activity toward SOM oxidation. Moreover, we will also probe the effects of size and morphology of the double perovskite supports on MOR performance.

To generate the targeted La_2NiMnO_6 perovskites with defined morphologies, we considered lessons learned from the prior literature. Specifically, various synthetic methods have already been used to generate double perovskites, such as but not limited to sol-gel,[34, 44-45] molten salt,[46-48] and hydrothermal protocols.[49] Though the sol-gel technique is commonly used in the literature for the synthesis of double perovskites, this technique often lacks proper control over

morphology, and yields poorly-defined nanoparticles. Similarly, nanoparticles generated with the molten salt synthesis method often tend to produce polydisperse particles in terms of both size and shape. By contrast, uniform nanowires possessing diameters around 200 nm have been reported for Y_2NiMnO_6, using a two-step hydrothermal method.[49] A relatively minor variation on the hydrothermal method has been utilized to synthesize LNMO and $LaCoO_3$ porous nanocubes with edge lengths ranging from 200-400 nm.[26, 50-51]

Considering this prior successful precedent in generating single perovskites with homogeneous size, shape, and morphology, we selected the hydrothermal methodology as an appropriate means of producing our desired family of single and double perovskites, characterized by a discrete morphology. Moreover, by rationally controlling reaction variables (including the nature of the reagents and additives used) within the hydrothermal method, we can correspondingly control the morphology of the perovskite supports. In this regard, we have reported on the successful fabrication of not only LNO, LMO, and LNMO nanocubes but also LNMO nanorods. In particular, we synthesized a series of (a) nanocubes of single and double perovskites, characterized by average diameters of ~200 nm, (b) additional double perovskite morphologies, measuring ~400 and 70 nm in diameter, and (c) LNMO nanorods with average diameters of ~50 nm. These findings were confirmed by both scanning electron microscopy (SEM) and transmission electron microscopy (TEM). We also used energy dispersive X-ray spectroscopy (EDS) and powder X-ray diffraction (XRD) to probe not only elemental composition but also the crystallinity of as-prepared perovskites.

Pt nanoparticles were subsequently deposited onto the external surfaces of these different perovskites to assess the electrocatalytic MOR performance of the resulting heterostructures. By comparison with the Pt/C standard, our as-prepared double perovskites yielded significantly

higher MOR activity with more than a 2-fold increase in activity as compared with Pt/C alone. Specifically, cyclic voltammetry data and trends in MOR performance suggest that the activity enhancement arises from a bifunctional effect involving the oxide surface.

We probed the discrete effects of varying composition, morphology, and particle size of the perovskite supports upon the resulting MOR performance. With respect to composition, X-ray photoelectron spectroscopy (XPS) results reveal that the addition of Ni to LNMO supports leads to a measurable shift in the Pt *d*-band to higher energies. This distinctive effect arising from favorable SMSI interactions within LNMO enabled a significant enhancement in MOR performance over the entire onset region, owing to the strong adsorption of oxygen species on Pt.

Regarding particle size, we examined the behavior of LNMO NCs with sizes spanning a range from 70 nm to 400 nm. These results reveal that catalytic activity increased by a factor of 1.5-fold with increasing particle size. Concerning morphology, we observed a similar 1.5-fold increase in MOR activity, when the particle architecture evolved from that of a symmetric cube to an anisotropic 'rod-like' motif. Our collective data highlight that particle size and morphology can have significant impacts upon key factors such as crystallinity, surface structure, oxygen vacancies, and surface termination. Although it is difficult to pin-point a single factor that can fully explain the trends in size and morphology, these results suggest that the higher degrees of crystallinity and surface order afforded by the larger particles and by the presence of anisotropic morphologies are conducive to improvements in MOR performance.

Results and Discussion

As a generalized protocol, all of the perovskite nanostructures were synthesized using a two-step procedure, wherein (i) an intermediate was generated by a hydrothermal reaction

followed by (ii) an annealing step to obtain the desired crystalline perovskite. For the synthesis of the perovskite nanocubes, we utilized a reasonably facile hydrothermal procedure, which has been previously utilized for the generation of LNO and $LaCoO_3$ perovskite nanocubes.[26, 50-53] This protocol was modified for our synthesis of LMO and LNMO nanocubes. In particular, we discovered that the synthesis of our Mn-based perovskite nanocubes requires a larger quantity of glycine and a higher pH, as compared with that used to generate LNO. In addition, we adapted another earlier reported hydrothermal method for the synthesis of Y_2NiMnO_6 nanorods to produce our desired LNMO nanorods, wherein the reported yttrium precursors were replaced with the more relevant lanthanum precursors used herein.[49]

Figure 1 depicts the powder XRD patterns of perovskite nanostructures, characterized by a rhombohedral structure, and these correspond well with what has been reported in the literature.[54-56] Specifically, the peaks at 2θ values of 23, 33, 40, 47, 53, and 58° correlate with the (012), (110) / (104), (202), (024), (116), and (214) planes, respectively, for all perovskites. Furthermore, the morphology of each perovskite structure was observed by both SEM and TEM, as highlighted in Figure 2 and summarized in Table 1. The porous nature of the perovskite nanocubes themselves is especially evident in the TEM images. The porous structure significantly increases the specific surface area of the particles, which is expected to be advantageous for their use as catalyst supports. The average edge lengths for the LNMO-8.7, LNMO-8.9, LNMO-9.3, LMO, and LNO NCs were measured to be 430 ± 113 nm, 181 ± 50 nm, 76 ± 21 nm, 191 ± 41 nm, and 245 ± 60 nm, respectively. Additionally, the LNMO NRs possessed average diameters of 43 ± 8 nm. The *d*-spacings obtained from the HRTEM images (Figures 2C, G, K and 3C, G, K) correspond with the expected (110) / (104) planes for all

perovskites. Selected area electron diffraction (SAED) patterns (Figures 2D, H, L and 3D, H, L) further confirm the crystallinity and structure of our as-prepared perovskite nanostructures.

Energy dispersive X-ray spectroscopy mapping images, as shown in Figure 4 and Figure S1, suggest that all elements are evenly dispersed throughout our LNMO NC, LNO NC, LMO NC, and LNMO NR samples. This finding is consistent with the XRD data and further confirms that we have achieved the desired chemical compositions at a homogeneous, uniform level within our as-prepared materials with neither crystalline or amorphous impurities apparent. In addition, quantitative SEM-EDS data (Figure S2) were collected for the LNMO-8.7 NCs, LNMO-8.9 NCs, LNMO-9.3 NCs, and LNMO NRs, all of which imply an elemental ratio associated with Mn: Ni of ~1: 1, in accordance with the expected stoichiometry for LNMO.

The surface areas of the various perovskite nanostructures are provided in Table 1 and were found to increase in the following order: LNMO-8.7 NCs < LNMO-8.9 NCs < LMO NCs < LNO NCs < LNMO NRs < LNMO-9.3 NCs. As expected, the LNMO-8.9 NCs, which possess the largest size, yielded the smallest surface area, whereas the LNMO-9.3 NCs, characterized by the smallest size, gave rise to the largest exposed surface area. In addition, the LNMO-8.9 NC, LMO NC, and LNO NC samples all appeared to maintain comparable surface areas, which is not surprising given their similar sizes and morphologies.

(A). Role of Reaction Parameters in the Synthesis of Nanocubes.

To form perovskite nanocubes (NCs), glycine and PVP were utilized as surfactants during the first step in terms of generating a reasonable intermediate species, as per prior protocols in this area. Specifically, glycine is used, because of its ability to act as both a chelating and a pore-forming agent which are essential towards enabling the formation of porous nanocubes. In addition, the function of PVP is as a surface stabilizing agent, aiding in the

production of colloidal nanostructures.[26, 57-58] XRD patterns of these as-prepared perovskites showed that La_2O_3 impurities also formed under these conditions. However, this extraneous material could be removed by washing with acetic acid (Figure S3A). It should be noted that a far more dilute acetic acid solution was used to wash the LNO samples in order to prevent sample dissolution. Nevertheless, SEM images of the LNMO-8.9, LMO, and LNO NC samples, prior to treatment with acetic acid, indicate that this 'cleaning' procedure is not destructive to the morphology, as shown in Figures S3B-D. Herein, all samples have been treated with acetic acid, unless otherwise stated.

In terms of general observations, as alluded to in the full and detailed Experimental section presented in the Supporting Information, in the synthesis of the perovskite nanocubes, the metal nitrate precursors are dissolved in water, thereby forming a six-coordinated complex with water.[50] Ammonia as a highly basic medium is used to control the pH of the reaction medium, which is important in terms of promoting the de-protonation of glycine and enabling the latter's coordination with the metal ions, thereby resulting in a metal-glycine complex. Therefore, finding the right ratio and balance of metal-to-glycine content is essential, because enough glycine must be present to fully coordinate with the metal complex. As such, the pH of the solution is important, because sufficient base is needed to react with glycine. The precise amount of base needed depended on the desired perovskite to be synthesized. Nevertheless, if the pH were to be too high, then the metals may potentially complex with the hydroxide ions (formed in situ) instead.[50] Additionally, PVP was used as another surfactant to further control the size and corresponding dispersion of the perovskite nanocubes. In order to fully understand the individual roles of the reactants, we have systematically altered the reaction variables/conditions and correlated these discrete parameters with changes in the resulting products.

Role of PVP: The role of PVP was investigated to determine its role in the reaction. XRD patterns indicate that pure LNMO is obtained, regardless of the amount of PVP used, as shown in Figure S4A. Moreover, it was observed that the precise amount of PVP had little to no apparent effect upon either morphology or size. For example, nanocubes with average sizes of 207 ± 16 nm, 181 ± 50 nm, and 264 ± 28 nm were formed when using 0, 300, and 600 mg of PVP, respectively, as shown in Figures S4B-D. For all of the samples discussed hereafter, we used 300 mg of PVP as a constant, during the synthesis process.

Role of Glycine: In accordance with previous reported procedures,[26, 52] LNO was successfully synthesized by using 4 mmol of glycine. However, for LNMO and LMO samples, we discovered that 4 mmol of glycine was insufficient in terms of generating the desired perovskite nanocubes. Therefore, in the case of LNMO, we systematically varied the amount of glycine from 0 mmol to 12 mmol, while keeping the pH constant at 8.9. In order to better understand the formation process and elucidate the effect of glycine, the as-prepared samples discussed within this section were not treated with acetic acid, so as to eliminate any interpretative confusion.

XRD patterns of the LNMO samples prepared with different amounts of glycine are shown in Figure S5A. These results indicate that when the glycine content is between 0 and 5 mmol, LNMO forms with a significant amount of impurities, which can likely be attributed to La_2O_3 and $La(OH)_3$. The amount of impurities significantly decreases when using 6 mmol of glycine, and are almost entirely removed at 7 mmol. Interestingly, the peaks attributed to La_2O_3 impurities intensify, when the amount of glycine is further increased to 8 and 12 mmol.

To ascertain the effect of glycine upon morphology, SEM images of the different samples were collected, as shown in Figures S5B-H. In the complete absence of glycine, spindles of La_2O_3 and/or $La(OH)_3$ impurities were produced with lengths of ~ 2 μm and diameters of ~250

nm. At relatively low amounts (up to 6 mmol) of glycine, irregular, polydisperse, micron-sized particles (primarily spheres) were generated. In fact, recognizably uniform nanocubes were not formed until 7 mmol of glycine was used, wherein the isolated sample consisted of nanocubes with average sizes of ~200 nm. Further increasing the amount of glycine content to 12 mmol still achieved the formation of nanocubes, but these were notably larger with a broader product size distribution. Hence, with these combined SEM and XRD results, we can assert that the amount of glycine is a key determinant of both the chemical composition and morphology of as-prepared LNMO. Based on these collective runs, 7 mmol was found to be the optimal quantity of glycine for the synthesis of LNMO NCs as the predominant, monodisperse motif, with little to no morphological or compositional impurities.

Similar results were observed in the context of the synthesis of LMO, as shown in Figure S6. At 4 mmol, there is a significant amount of La_2O_3 impurities along with the formation of micron-scale spheres and spindles. At 8 mmol, the isolated sample was primarily characterized by nanocubes with average sizes of ~250 nm. Therefore, on the basis of these experiments, we chose 8 mmol as the optimal amount of glycine required for the production of LMO NCs.

It is clear that a larger amount of glycine is necessary to induce the formation of Mn-containing perovskites as compared with LNO alone. This requirement of having to achieve a sufficiently high enough, ‘threshold’ amount of glycine can likely be attributed to the lower stability of the Mn-based-glycine complex, as compared with either analogous Ni- or La-based-glycine complexes.[59] At insufficiently low glycine levels, the necessary precursor metal-glycine complexes either do not materialize at all or are unstable. Nevertheless, as we noted, an excess of glycine may result in competing polymerization processes, which may lead to a higher degree of polydispersity, denoting a less desirable outcome. Moreover, it should be noted that glycine

likely combusts and decomposes during the annealing step and can therefore function as a 'catalyst' with which to promote the synthesis of the desired perovskites at a relatively lower annealing temperature than otherwise would have been possible.[60-61] Not surprisingly, this assertion may further explain the fairly reduced yield of perovskites in the presence of comparatively low amounts of glycine. We summarize our findings in the SI section.

Role of pH: For all perovskites studied herein, we noticed that the exact magnitude of pH used was a significant determinant of particle size, thereby indicating that the synthesis process was particularly pH sensitive. In particular, we found that LNMO and LMO both necessitated a higher pH to promote purity and growth, as compared with LNO.

For LNMO, the pH was varied between 8.2 and 9.3. XRD patterns (Figure 5A) of the samples, synthesized under different pH values, all were consistent with the generation of pure LNMO. Moreover, as shown in Figures 5B-J, nanocubes were formed at all of these pH readings. However, the apparent size was inversely proportional (albeit nonlinearly) to pH. A similar set of findings characterized our experimental results with LMO and LNO, as shown in Figures S7 and S8, respectively. From the prior literature, a comparable conclusion was noted for $LaCoO_3$ nanocubes, that had been generated under a similar synthesis procedure.[50] Furthermore, it should be remarked that for all perovskite systems studied herein, the presence of a nanocube morphology is less apparent at higher pH, a finding which may be related with the associated smaller sizes detected. This scenario was especially notable for LMO synthesized with a pH of 9.3 and LNO produced at a pH of 7.8, whereby particles, lacking a well-defined cubic morphology but characterized by average sizes of 28 ± 4 and 52 ± 12 nm, respectively, were observed. By contrast, it was determined that NCs with sizes of ~200 nm could be reliably synthesized for LNMO, LMO, and LNO using a pH of 8.9, 8.7, and 7.4, respectively.

The synthesis of LMO and LNMO NCs of similar sizes apparently requires a higher pH as compared with LNO. We can potentially ascribe these observations to the comparatively lower stability of Mn-glycine complexes as compared with the analogous Ni-glycine complex. In addition, the influence of pH on the formation of the perovskite NCs can likely be further explained by changes within the chemical bonding structure of glycine, at different pH values. We further elaborate upon our thoughts on this issue in the SI section.

(B). Role of Reaction Parameters in the Synthesis of Nanorods and Nanowires.

For the synthesis of the LNMO nanorods, as implied in the Experimental section, the metal salt precursors were first dissolved in water. Next, an aqueous solution of NaOH was added to the solution so as to induce precipitation of metal hydroxides, which were then subjected to a hydrothermal treatment. After the hydrothermal reaction, individual, isolated metal hydroxide composite nanowires were formed, as shown in Figure S9, and these were subsequently annealed at higher temperatures to form the desired perovskites.

We systematically varied a number of different complementary reaction parameters, including (a) solvent, (b) reaction time, (c) additive and precursor identity, and (d) hydrothermal reaction temperature, in our series of experiments and observed their discrete effects upon the morphology of the isolated intermediates. However, SEM images of the isolated intermediates (Figure S10) indicate that changing these specific parameters were not particularly effective in precisely tuning the morphology, size, and composition, simultaneously. A more detailed discussion of these reaction variables is provided in the Supporting Information.

Nevertheless, in terms of the more relevant and tunable parameters, we found that (e) the annealing temperature in addition to (f) alterations in the base identity (and associated amounts) turned out to be more important and impactful. As a notable reminder, in this reaction, the base

acts as both the precipitating agent and the mineralizer during the hydrothermal reaction, which can functionally influence the as-generated morphology.[62] Hence, we carefully investigated the effects of both the annealing temperature and the identity of the base (and base quantities) as viable means of controlling not only the as-produced nanowire/nanorod morphology but also their corresponding diameters, given the significance of obtaining simultaneously well-defined *sizes and shapes* of our nanostructures for our subsequent MOR experiments.

Role of Base: Previous reports for other metal oxides, apart from double perovskites, indicate that changing the identity of the base used in similar hydrothermal processes can definitely influence the size of the desired oxides.[62-63] Inspired by these reports, we synthesized LNMO nanorods using NaOH, KOH, LiOH, and NH_4OH as the various bases, in an attempt to achieve fine control over morphology. The XRD patterns of the final products after annealing at 1000°C, Figure S11, reveal that all of the bases attempted lead to the formation of the desired structure. However, LiOH yielded a significant amount of La_2O_3 impurities, though these could likely be washed out by acetic acid.

We analyzed the morphologies of the intermediate nanowires in order to better determine the effect of the base upon the resulting morphology. Indeed, we found that altering the base identity itself had little if any apparent effect upon morphology, since NaOH, KOH, and LiOH all gave rise to nanowires and nanorods. The accompanying SEM images (Figure S12) of the different samples highlight nanorods with average diameters of 50 ± 12, 29 ± 5, 31 ± 4, and 32 ± 11 nm, created when NaOH, KOH, LiOH, and NH_4OH were respectively used. It should be noted however that while the diameters of the NaOH sample appeared to be slightly larger than those of the other samples, there was no significant correlation with size. These results indicate that changing the base cannot be necessarily used as a method to manipulate the apparent

dimensionality over a wide range of the as-prepared LNMO nanorods. As such, we chose NaOH as the preferred base to be used in further experiments, as it can yield high-quality nanorods with longer lengths as compared with those generated using other bases.

Role of Annealing Temperature: We sought to determine the optimal annealing temperature required to form the desired LNMO nanorods. In so doing, we varied annealing temperatures in the range of 600 to 1000°C. The XRD patterns of the nanorods annealed at different temperatures, without the acetic acid washing step, are shown in Figure S13, which indicates that the desired perovskite structure is capable of being formed at temperatures as low as 600°C. Minor impurities that can be ascribed to La_2O_3 are present in the samples annealed at 600 and 700°C but are completely removed at the higher temperatures. In addition, it should be noted that these impurities can be removed by washing with acetic acid.

SEM images (presented in Figure S14) were taken of each sample to determine the effect of annealing temperature upon morphology. At annealing temperatures of 600, 700, and 800°C, the nanorod morphology is still evident, and each sample exhibits average diameters, ranging from ~40 to 60 nm. At 900°C, whereas measured diameters rise to ~ 68 ± 12 nm, the nanorods themselves begin to fragment, thereby leading to the formation of irregular particles. At 1000°C, though isolated nanorods are observed with average diameters of as much as ~93 ± 15 nm, the nanorods themselves are almost completely destroyed. The larger particle sizes observed at 900 and 1000°C are likely caused by aggregation and sintering effects. From these collective results, we determined that 800°C represented an optimal annealing temperature, because pure LNMO nanorods are formed at this temperature with the desired, intact anisotropic morphology.

Characterization of Perovskite / Pt Catalysts:

To investigate the discrete effects of both the chemical composition and morphology of a catalyst support within the methanol oxidation reaction, we have deposited Pt nanoparticles onto the surfaces of the variously formed La-based perovskites. Specifically, Pt nanoparticles were deposited onto the surfaces of the perovskites by reducing the Pt precursor with $NaBH_4$ in the presence of these oxide support materials. All samples were characterized by HRTEM and SAED, as shown in Figure 6 and 7. For all of the samples, Pt nanoparticles with average sizes of about 2-4 nm were found to have been immobilized onto the outer surfaces of the perovskites, as indicated in Figure 5. Moreover, HRTEM data were used to measure the *d*-spacings of these Pt nanoparticles for all samples; these readings were found to center on 0.23 nm, which can be ascribed to the Pt (111) plane. In addition, the corresponding SAED confirms the simultaneous presence of both the perovskite supports and the Pt nanoparticles themselves.

XPS was used to probe the nature of chemical states and the extent of electronic interactions between the perovskite supports and the Pt nanoparticles. Specifically, the survey spectra for all of the samples tested are shown in Figure S17, indicating the presence of all of the expected elements with no noticeable impurities apparent.

The O 1*s* peaks for all of the samples are provided in Figure S18 with the data summarized in Table S1. All of these samples incorporate peaks which are found at binding energies of ~528.5, 529.5, and 531.8 eV. We note that the two peaks detected at the lower energies are assigned to the lattice oxygen, whereas the other peak can be ascribed to hydroxyl groups localized on the surface. The LMO, LNO, LNMO-8.7, and LNMO NR samples all maintain additional peaks at higher energies in the vicinity of 532 eV, which are likely caused by the presence of adsorbed H_2O. Moreover, the LNMO-8.7 and LNMO NR samples both maintain two additional peaks, located at ~526.7 and 530.6 eV, the latter of which are likely associated

with adsorbed oxygen (O_{ads}) species on the surface. The magnitude of the O_{ads} peak has been ascribed to a measure of oxygen vacancy content, wherein an increase in the peak intensity can be correlated with a corresponding increase in the number of oxygen vacancies.

The chemical state of La was investigated by measuring the La 3*d* peak, as shown in Figure S19, and these data are summarized in Table S2. It is important to note that the La $3d_{3/2}$ peak also overlaps with the Ni $2p_{3/2}$ peak, which can thereby render the deconvolution and corresponding interpretation of the peaks as rather complicated. Both of the La $3d_{5/2}$ and $3d_{3/2}$ signals split into two peaks, which emanate from a core-hole state, $3d^14f^0$, in addition to a core hole state with an electron transferred from the oxygen 2*p* valence band to the empty 4f orbital, yielding $3d^14f^1$.[64-65] The La $3d_{5/2}$ peaks are situated between ~830 and 842 eV for all samples analyzed. Within this region, all of the samples possess a main La $3d_{5/2}$ peak, centered at ~835-836 eV, in addition to a satellite peak, located at ~838-839 eV. The distance between the two La $3d_{5/2}$ peaks is expected to be ~4.6 eV for La_2O_3. However, within our double perovskites, the measured peak separation in this region is actually in the range between 3.2 and 3.3 eV. The positions of these peaks, coupled with the measured energy gap between the main peaks and the satellite peaks, are closer to what would have been expected for $La(OH)_3$ as opposed to La_2O_3, a finding which is consistent with results derived from the O 1s spectra.

It is worth emphasizing that additional peaks were observed within the La 3*d* region for both LNMO-8.7/Pt and LNMO NRs/Pt samples, which were not present in the other materials analyzed. These peaks, situated at 832.3 and 833.4 for LNMO-8.7/Pt and LNMO NRs/Pt, respectively, could potentially be assigned to another La species. Interestingly, in these samples, the measured energy gaps between the main peak and satellite peak are in the range of ~3.9 eV. Because of the shift towards lower energies along with the larger apparent energy gap, it is

plausible that these peak features can be ascribed to either La_2O_3 or similar types of oxides within these perovskites.[66] Whereas the observed energy gap remains smaller than what might have been expected for La_2O_3, we hypothesize this noticeably lower set of values may be caused by the presence of carbon and oxygen species adsorbed onto the surface.[67] Overall, these results tend to indicate that the LNMO-8.7/Pt and LNMO NRs/Pt are 'special' cases, in that these particular samples possess a different surface structure as compared with that of the other samples. The inference is that LNMO-8.7/Pt and LNMO NRs/Pt are not necessarily entirely covered by and coated with hydroxyl groups; in fact, other oxygen-containing species may also co-exist with implications for electrochemical activity.

The Ni-containing perovskites all possess an additional peak, which is not observed in LMO but which appears in the region between ~552 and 557 eV and likely corresponds with the presence of Ni^{2+}/Ni^{3+} species. It is expected that the peaks located at lower binding energies are indicative of a higher amount of Ni^{2+} species present, whereas a shift to higher binding energies signals the reverse, i.e. the presence of more Ni^{3+} species. From our analysis, we determined the following trend in the behavior of the binding energy value of the Ni peak: LNMO-8.7/Pt > LNMO NRs/Pt > LNO/Pt > LNMO-8.9/Pt > LNMO-9.3/Pt. Though the Ni^{3+} oxidation state is necessary for the successful formation of our Ni-based perovskite structures, the LNMO double perovskites can more flexibly accommodate for a range of variations in the Ni oxidation state, because Mn can exist as both Mn^{3+} and Mn^{4+} species. It is expected therefore that an increase in Ni^{2+} would lead to (i) a growth in the number of oxygen vacancies and/or (ii) an increase in the Mn^{4+} oxidation state, both of which can give rise to an improved electrocatalytic activity.

As shown in Figure 6, the Pt 4*d* peaks were measured by XPS to probe the effect of the underlying perovskite support on the *d*-band of the Pt nanoparticles. The position of the $4d_{5/2}$

peak in elemental, bulk platinum is 315 eV.[68] Deposition of Pt onto the LMO sample does not lead to a significant shift in the peak position. However, deposition of platinum onto the analogous LNMO and LNO samples leads to significant downshifts in the binding energy of up to 3.3 eV. It was observed that the position of the Pt $4d_{5/2}$ peak decreases in magnitude in the following order: LMO > LNMO-9.3 > LNO > LNMO-8.7 ≈ LNMO 8.9 > LNMO NRs. That is, a larger shift in the binding energy would be indicative of a stronger electronic interaction between the Pt catalyst and the underlying oxide perovskite support.

On the basis of these results, the addition of Ni within the perovskites clearly yields a significant effect upon the electronic properties of Pt, whereas oxides containing only Mn do not appreciably affect Pt to such a measurable extent. A decrease in the binding energy suggests that the Pt *d*-band is shifted to higher energies, which would be expected to lead to stronger interactions with oxygen adsorbates. That is, a desirable electron transfer from the oxide support to the Pt is favorable for small organic molecule oxidation, because oxygen adsorbates are necessary to catalyze the oxidation and removal of partially oxidized intermediates.[69-70]

Electrochemical Activity:

General Observations: CV curves for each of the catalysts, along with a Pt/C standard, were collected in an Ar-saturated solution of 0.1 M perchloric acid, using a scan rate of 20 mV/s. Representative CV curves, corresponding to samples of LNO/Pt, LMO/Pt, LNMO-8.7/Pt, LNMO-8.9/Pt, LNMO-9.3/Pt, LNMO NRs/Pt, and Pt/C, respectively, are provided in Figure 7. CV curves for all of the samples possess a distinctive shape, which is expected for nanostructured Pt.[71] Specifically, the hydrogen adsorption region is observed between 0 to 0.3 V and the reversible surface oxidation of Pt can be observed at potentials above 0.6 V. The CV

curves corresponding to Pt-decorated LNO and LNMO-8.9 NCs maintain very similar shapes, especially within the Pt oxidation region.

By contrast, the analogous CV curve for LMO/Pt displays a unique and characteristic suppression of the oxide region. This is consistent with the XPS results, which revealed that the oxides, incorporating Ni, shift the Pt *d*-band to higher energies and should thereby lead to stronger oxygen adsorption, whereas the use of LMO alone did not lead to a significant shift in the *d*-band. The apparent suppression of oxide formation on Pt in LMO is consistent with the lower activity for the methanol oxidation reaction observed for this catalyst as compared with the analogous Ni-containing perovskites, since adsorption of oxygen species is essential, especially for the removal of poisoning CO species.

In terms of accounting for the effect of support composition, the oxide reduction peaks for the Ni-containing perovskites were observed at ~800 mV. The fact that there is little difference in the measured peak locations among the various different individual perovskite supports would imply that the changes in either chemical composition or morphology within these oxides may have little effect upon the magnitude of the observed metal-support interactions. When these results are combined with the complementary XPS data, these observations suggest that the down-shift in the Pt *d*-band is significant in determining the nature of the electrochemical properties of the Pt deposited onto the oxides. The relative magnitudes of these down-shifts, resulting from the composition and morphology, are less significant. By contrast, the peak position for Pt/C is situated at ~730 mV, which is significantly shifted to lower potentials relative to the perovskite supports themselves. This noticeable difference in behavior suggests that the oxides lead to an intrinsically different type of metal-support interaction as compared with carbon support controls. What is apparent is that the consistent increase in peak

position noted for the perovskites in general indicates that oxygen likely binds more weakly to the Pt immobilized onto the perovskites as opposed to the analogous Pt/C control system.

Judging from the relative peak positions alone, the significant shift in the position of the oxide reduction peak to lower potentials in Pt/C would be indicative of higher MOR performance. However, this finding in and of itself does not account for the relative surface chemistry of the support materials. The oxide surfaces of the perovskite supports provide for oxygen species at the metal oxide-interface over the entire potential window. Thus, CO oxidation can proceed via a bi-functional process at the Pt-oxide interface at low overpotentials without necessarily requiring a high surface coverage of oxygen species to be present on Pt at higher overpotentials. By contrast, conventional carbon supports provide for far fewer oxygen species at the Pt-support interface, and therefore, CO oxidation in that case is dependent upon the formation of oxide species via Pt surface oxidation.

Specific Findings: The activity of each catalyst towards MOR was measured by taking linear sweep voltammetry (LSV) curves within an Ar-saturated 0.1 M perchloric acid solution containing 0.5 M methanol. The results were normalized to the Pt ECSA, and are displayed in terms of the specific activity. To understand the *effect of chemical composition* upon activity, the data for LMO/Pt, LNO/Pt, LNMO-8.9/Pt, and Pt/C samples are compared and contrasted in Figure 8A, B. It is apparent that all of the perovskite supports outperform the Pt/C standard over the entire onset region, which indicates that the metal oxides are superior supports as compared with carbon. It should be noted that when the perovskites themselves were used as the functional catalyst without any Pt present at all, there was no apparent electrocatalytic activity detected. When these observations are combined with the CV data, the results suggest that the increase in

MOR activity arises from a bifunctional process, wherein the use of perovskites facilitates CO oxidation, which minimizes unwanted CO poisoning at the Pt active sites.

At a reaction potential of 0.8 V, LNO/Pt evinces activities that are about 1.3 and 2.4 times higher than those of LMO/Pt and Pt/C, respectively; furthermore, these readings are comparable in magnitude to that of LNMO-8.9/Pt. Thus, the incorporation of Ni within LMO to yield LNMO can increase the performance of the double perovskite as compared with pristine LMO alone. Specifically, the increase in MOR activity resulting from the addition of Ni within LNMO/Pt can be attributed to the measurable shift in the Pt *d*-band and therefore stronger oxygen binding than would have the case with LMO/Pt alone.

To understand *the effects of both size and morphology*, the MOR results for LNMO NRs and NCs characterized by various sizes are compared in Figure 8C, D. The results are complicated in that the net outcomes of these two parameters appear to be intertwined and interdependent. To determine the specific influence of size, we compared the activity of LNMO NC supports across sizes that vary from 70 nm to 400 nm. Interestingly, the specific activity rises from 0.58 mA cm^{-2} to 0.75 mA cm^{-2}, as the size of the particle is correspondingly increased from 70 nm to 400 nm. This result is somewhat counterintuitive, since higher activity is often associated with increases in the catalytically available and accessible surface area, as the particle size is decreased. However, in our case, the size of the Pt nanoparticle catalyst remains constant regardless of the support size and, hence, the size-dependent effect must therefore arise from the influence of the support size upon the observed catalyst-support interactions.

The size of the metal oxide nanoparticles can affect several key parameters that may impact upon catalytic performance. First, increasing the size of the perovskite support should lead to corresponding increases in the crystallinity of the particle and the uniformity of the oxide

surface. In addition, the size of the particle can also influence the surface energy, the structure of the surface termination, the extent of oxygen vacancies, and the degree of Ni^{2+} exposure at the surface. Although it is difficult to ascribe the overarching importance of any one parameter, it is evident that larger particle sizes can lead to a desirable surface structure that induces a favorable metal-support interaction for MOR oxidation.

To analyze the influence of particle morphology, we compared the activity of Pt NPs supported onto LNMO NC and NR possessing comparable diameters of 70 nm and 50 nm, respectively. In particular, the LNMO NRs yielded higher performance over the entire onset region. At 0.8 V, the specific activity of the NRs was measured to be ~1.5 times larger than that of the NCs. By analogy with particle size, morphology can impact upon the crystallinity and surface structure. Specifically, one-dimensional nanorods can selectively display certain active facets oriented along their anisotropic axis. Moreover, unlike what was observed for the porous nanocubes, the nanorods possess a smooth, non-porous surface, as indicated by our HRTEM data, which may also contribute to the observed differences in activity between these morphologies. Overall, these results suggest that the anisotropic 1D morphology of the nanorods appear to lead to improvements in MOR activity as compared with isotropic nanocube motifs.

Conclusions

LNO, LMO, and LNMO nanocubes were synthesized by a simple, surfactant-assisted hydrothermal method. The use of glycine was crucial for the formation of nanocubes, a structural motif that had not been previously generated for these chemical compositions in past studies. Moreover, the sizes of these nanocubes could be manipulated by precisely and carefully controlling the pH of the reaction medium. As such, we were able to generate these three

different oxide perovskites as nanocubes possessing average sizes of ~200 nm; furthermore, we created additional LNMO nanocubes with sizes in the range of ~70 to 400 nm. Moreover, to the best of our knowledge, we are the first to produce analogous LNMO nanorods with average diameters of ~ 50 nm using a surfactant-less hydrothermal method. The chemical composition, crystallinity, and observed morphology of all of our samples were characterized by a synergistic combination of XRD, SEM, HRTEM, and EDS.

The electrochemical performance of Pt deposited onto these as-prepared perovskites as supports for the electrocatalytic oxidation of methanol was systematically investigated. Our double perovskites consistently exhibited activities, which were more than double that of the Pt/C commercial standard. This higher observed activity is likely caused by a bifunctional mechanism, wherein the surfaces of the perovskites facilitate CO oxidation so as to reduce unfavorable CO poisoning at the Pt active sites.

A comparison between LNO, LMO, and LNMO nanocubes was performed to understand the influence of chemical composition upon electrocatalytic performance. Because LNO and LNMO yielded comparable activities which are about 1.3x higher than that of LMO, these findings indicate that the presence of Ni most likely leads to better catalytic performance. This activity dependence on chemical composition was corroborated by XPS results which are consistent with a higher shift in the position of the Pt's *d*-band energy upon interaction with Ni-containing perovskites as opposed to analogous Mn-containing perovskites such as LMO.

To deduce the effect of size upon the activity of the LNMO nanocubes, we compared activity values across a range spanning 70 to 400 nm; the measured activity clearly rose with increasing perovskite particle size, which suggests that the presence of a larger particle size may induce the creation of a surface structure which induces favorable metal-support interactions.

Finally, to understand the role of morphology, we compared the performance of 70 nm nanocubes versus 50 nm nanorods of LNMO. The anisotropic motifs achieved 1.5x higher activity values as compared with their isotropic analogues. This evident increase in activity may be attributed to the anisotropic nature of the nanorods, which can not only selectively display specific active facets but also promote advantageous surface crystallinity and structure in order to promote more favorable SMSIs.

As such, this overall study herein highlights a rational means with which chemical composition, size, and morphology can be systematically and rationally used to tune and manipulate metal-support interactions. These advances will enable the predictive development of highly active, electrocatalytically relevant catalyst-support systems.

Conflicts of Interest

There are no conflicts to declare.

Acknowledgements

This material is based on work supported by the U.S. National Science Foundation under Grant No. CHE-1807640. Structural characterization experiments (TEM, SEM, and XPS) for this manuscript were performed in part at the Center for Functional Nanomaterials, located at Brookhaven National Laboratory, which is supported by the U.S. Department of Energy under Contract No. DE-SC0012704.

References

1. Shao, Y.; Yin, G.; Gao, Y., Understanding and approaches for the durability issues of Pt-based catalysts for PEM fuel cell. *J. Power Sources* **2007,** *171* (2), 558-566.
2. Yoon, S.; Oh, K.; Liu, F.; Seo, J. H.; Somorjai, G. A.; Lee, J. H.; An, K., Specific Metal-Support Interactions between Nanoparticle Layers for Catalysts with Enhanced Methanol Oxidation Activity. *ACS Catal.* **2018,** *8* (6), 5391-5398.
3. Su, N.; Hu, X.; Zhang, J.; Huang, H.; Cheng, J.; Yu, J.; Ge, C., Plasma-induced synthesis of Pt nanoparticles supported on TiO_2 nanotubes for enhanced methanol electro-oxidation. *Appl. Surf. Sci.* **2017,** *399*, 403-410.
4. Hua, H.; Hu, C.; Zhao, Z.; Liu, H.; Xie, X.; Xi, Y., Pt nanoparticles supported on submicrometer-sized TiO_2 spheres for effective methanol and ethanol oxidation. *Electrochim. Acta* **2013,** *105*, 130-136.
5. Antolini, E., Photo-assisted methanol oxidation on Pt-TiO_2 catalysts for direct methanol fuel cells: A short review. *Appl. Catal., B* **2018,** *237*, 491-503.
6. Li, H.; Liu, S.; Wang, X.; Zu, G.; Li, D.; Wang, J.; Zhao, J., Platinum nano-flowers with controlled facet planted in titanium dioxide nanotube arrays bed and their high electro-catalytic activity. *Sustainable Mater. Technol.* **2019,** *20*, e00093.
7. Pietron, J. J.; Pomfret, M. B.; Chervin, C. N.; Long, J. W.; Rolison, D. R., Direct methanol oxidation at low overpotentials using Pt nanoparticles electrodeposited at ultrathin conductive RuO_2 nanoskins. *J. Mater. Chem.* **2012,** *22* (11), 5197-5204.
8. An, G.-H.; Lee, E.-H.; Ahn, H.-J., Ruthenium and ruthenium oxide nanofiber supports for enhanced activity of platinum electrocatalysts in the methanol oxidation reaction. *Phys. Chem. Chem. Phys.* **2016,** *18* (22), 14859-14866.
9. Rajeswari, J.; Viswanathan, B.; Varadarajan, T. K., Tungsten trioxide nanorods as supports for platinum in methanol oxidation. *Mater. Chem. Phys.* **2007,** *106* (2-3), 168-174.
10. Micoud, F.; Maillard, F.; Gourgaud, A.; Chatenet, M., Unique CO-tolerance of Pt-WO_x materials. *Electrochem. Commun.* **2009,** *11* (3), 651-654.
11. Ganesan, R.; Lee, J. S., An electrocatalyst for methanol oxidation based on tungsten trioxide microspheres and platinum. *J. Power Sources* **2006,** *157* (1), 217-221.
12. Wang, Y.-J.; Wilkinson, D. P.; Zhang, J., Non-carbon Support Materials for Polymer Electrolyte Membrane Fuel Cell Electrocatalysts. *Chem. Rev.* **2011,** *111* (12), 7625-7651.
13. Penner, S.; Armbrüster, M., Formation of Intermetallic Compounds by Reactive Metal–Support Interaction: A Frequently Encountered Phenomenon in Catalysis. *ChemCatChem* **2015,** *7* (3), 374-392.
14. Lan, A.; Mukasyan, A. S., Complex $SrRuO_3$−Pt and $LaRuO_3$−Pt Catalysts for Direct Alcohol Fuel Cells. *Ind. Eng. Chem. Res.* **2008,** *47* (23), 8989-8994.
15. Ho, V. T. T.; Nguyen, N. G.; Pan, C.-J.; Cheng, J.-H.; Rick, J.; Su, W.-N.; Lee, J.-F.; Sheu, H.-S.; Hwang, B.-J., Advanced nanoelectrocatalyst for methanol oxidation and oxygen reduction reaction, fabricated as one-dimensional pt nanowires on nanostructured robust Ti0.7Ru0.3O2 support. *Nano Energy* **2012,** *1* (5), 687-695.
16. Ho, V. T. T.; Pillai, K. C.; Chou, H.-L.; Pan, C.-J.; Rick, J.; Su, W.-N.; Hwang, B.-J.; Lee, J.-F.; Sheu, H.-S.; Chuang, W.-T., Robust non-carbon Ti0.7Ru0.3O2 support with co-catalytic functionality for Pt: enhances catalytic activity and durability for fuel cells. *Energy Environ. Sci.* **2011,** *4* (10), 4194-4200.

17. Moghaddam, R. B.; Pickup, P. G., Support effects on the oxidation of methanol at platinum nanoparticles. *Electrochem. Commun.* **2011,** *13* (7), 704-706.
18. Li, L.; Tan, S.; Salvatore, K. L.; Wong, S. S., Nanoscale Perovskites as Catalysts and Supports for Direct Methanol Fuel Cells. *Chem. - Eur. J.* **2019,** *25* (33), 7779-7797.
19. Lan, A.; Mukasyan, A. S., Perovskite-Based Catalysts for Direct Methanol Fuel Cells. *J. Phys. Chem. C* **2007,** *111* (26), 9573-9582.
20. Pena, M. A.; Fierro, J. L. G., Chemical Structures and Performance of Perovskite Oxides. *Chem. Rev.* **2001,** *101* (7), 1981-2017.
21. Levasseur, B.; Kaliaguine, S., Effect of the rare earth in the perovskite-type mixed oxides $AMnO_3$ (A = Y, La, Pr, Sm, Dy) as catalysts in methanol oxidation. *J. Solid State Chem.* **2008,** *181* (11), 2953-2963.
22. Levasseur, B.; Kaliaguine, S., Methanol oxidation on $LaBO_3$ (B=Co, Mn, Fe) perovskite-type catalysts prepared by reactive grinding. *Appl. Catal., A* **2008,** *343* (1-2), 29-38.
23. Zhu, K.; Shi, F.; Zhu, X.; Yang, W., The roles of oxygen vacancies in electrocatalytic oxygen evolution reaction. *Nano Energy* **2020,** *73*, 104761.
24. Zhou, X.; Hu, B.; Chen, Z.; Delgado, F.; Srivastava, R., Nonprecious Metal Perovskite Electrocatalysts for Direct Methanol Fuel Cells. *Electrochem. Solid-State Lett.* **2005,** *8* (11), A616-A618.
25. Yavari, Z.; Noroozifar, M.; Khorasani-Motlagh, M., Multifunctional catalysts toward methanol oxidation in direct methanol fuel cell. *J. Appl. Electrochem.* **2015,** *45* (5), 439-451.
26. Yu, N.; Kuai, L.; Wang, Q.; Geng, B., Pt nanoparticles residing in the pores of porous $LaNiO_3$ nanocubes as high-efficiency electrocatalyst for direct methanol fuel cells. *Nanoscale* **2012,** *4* (17), 5386-5393.
27. Scofield, M. E.; Koenigsmann, C.; Bobb-Semple, D.; Tao, J.; Tong, X.; Wang, L.; Lewis, C. S.; Vukmirovic, M. B.; Zhu, Y.; Adzic, R. R.; Wong, S. S., Correlating the chemical composition and size of various metal oxide substrates with the catalytic activity and stability of as-deposited Pt nanoparticles for the methanol oxidation reaction. *Catal. Sci. Technol.* **2016,** *6* (7), 2435-2450.
28. Tiano, A. L.; Santulli, A. C.; Koenigsmann, C.; Feygenson, M.; Aronson, M. C.; Harrington, R.; Parise, J. B.; Wong, S. S., Toward a Reliable Synthesis of Strontium Ruthenate: Parameter Control and Property Investigation of Submicrometer-Sized Structures. *Chem. Mater.* **2011,** *23* (14), 3277-3288.
29. Meher, S. K.; Rao, G. R., Morphology-controlled promoting activity of nanostructured MnO_2 for methanol and ethanol electrooxidation on Pt/C. *J. Phys. Chem. C* **2013,** *117* (10), 4888-4900.
30. Pal, S.; Sharada, G.; Goyal, M.; Mukherjee, S.; Pal, B.; Saha, R.; Sundaresan, A.; Jana, S.; Karis, O.; Freeland, J. W.; Sarma, D. D., Effect of anti-site disorder on magnetism in La_2NiMnO_6. *Phys. Rev. B* **2018,** *97* (16), 165137.
31. Nasir, M.; Khan, M.; Kumar, S.; Bhatt, S.; Patra, N.; Bhattacharya, D.; Jha, S. N.; Biring, S.; Sen, S., The effect of high temperature annealing on the antisite defects in ferromagnetic La_2NiMnO_6 double perovskite. *J. Magn. Magn. Mater.* **2019,** *483*, 114-123.
32. Matte, D.; de Lafontaine, M.; Ouellet, A.; Balli, M.; Fournier, P., Tailoring the magnetocaloric effect in La_2NiMnO_6 thin films. *Phys. Rev. Appl.* **2018,** *9* (5), 054042.
33. Bernal-Salamanca, M.; Konstantinovic, Z.; Balcells, L.; Pannunzio-Miner, E.; Sandiumenge, F.; Lopez-Mir, L.; Bozzo, B.; Herrero-Martin, J.; Pomar, A.; Frontera, C.;

Martinez, B., Nonstoichiometry Driven Ferromagnetism in Double Perovskite $La_2Ni_{1-x}Mn_{1+x}O_6$ Insulating Thin Films. *Cryst. Growth Des.* **2019,** *19* (5), 2765-2771.
34. Tong, Y.; Wu, J.; Chen, P.; Liu, H.; Chu, W.; Wu, C.; Xie, Y., Vibronic Superexchange in Double Perovskite Electrocatalyst for Efficient Electrocatalytic Oxygen Evolution. *J. Am. Chem. Soc.* **2018,** *140* (36), 11165-11169.
35. Lee, D.-G.; Gwon, O.; Park, H.-S.; Kim, S. H.; Yang, J.; Kwak, S. K.; Kim, G.; Song, H.-K., Conductivity-Dependent Completion of Oxygen Reduction on Oxide Catalysts. *Angew. Chem., Int. Ed.* **2015,** *54* (52), 15730-15733.
36. Jiang, M.; Li, J.; Zhao, Y.; Pan, L.; Cao, Q.; Wang, D.; Du, Y., Double Perovskites as Model Bifunctional Catalysts toward Rational Design: The Correlation between Electrocatalytic Activity and Complex Spin Configuration. *ACS Appl. Mater. Interfaces* **2018,** *10* (23), 19746-19754.
37. Hua, B.; Zhang, Y.-Q.; Yan, N.; Li, M.; Sun, Y.-F.; Chen, J.; Li, J.; Luo, J.-L., The Excellence of Both Worlds: Developing Effective Double Perovskite Oxide Catalyst of Oxygen Reduction Reaction for Room and Elevated Temperature Applications. *Adv. Funct. Mater.* **2016,** *26* (23), 4106-4112.
38. Wang, H.; Wang, J.; Pi, Y.; Shao, Q.; Tan, Y.; Huang, X., Double Perovskite $LaFe_xNi_{1-x}O_3$ Nanorods Enable Efficient Oxygen Evolution Electrocatalysis. *Angew. Chem., Int. Ed.* **2019,** *58* (8), 2316-2320.
39. Liu, Y.; Wang, Z.; Veder, J.-P. M.; Xu, Z.; Zhong, Y.; Zhou, W.; Tade, M. O.; Wang, S.; Shao, Z., Highly Defective Layered Double Perovskite Oxide for Efficient Energy Storage via Reversible Pseudocapacitive Oxygen-Anion Intercalation. *Adv. Energy Mater.* **2018,** *8* (11), 1702604.
40. Hou, Y.-C.; Ding, M.-W.; Liu, S.-K.; Wu, S.-K.; Lin, Y.-C., Ni-substituted $LaMnO_3$ perovskites for ethanol oxidation. *RSC Adv.* **2014,** *4* (11), 5329-5338.
41. Gaikwad, V. M.; Yadav, K. K.; Sunaina; Chakraverty, S.; Lofland, S. E.; Ramanujachary, K. V.; Nishanthi, S. T.; Ganguli, A. K.; Jha, M., Design of process for stabilization of La_2NiMnO_6 nanorods and their magnetic properties. *J. Magn. Magn. Mater.* **2019,** *492*, 165652.
42. Nasir, M.; Khan, M.; Bhatt, S.; Bera, A. K.; Furquan, M.; Kumar, S.; Yusuf, S. M.; Patra, N.; Bhattacharya, D.; Jha, S. N.; Liu, S.-W.; Biring, S.; Sen, S., Influence of Cation Order and Valence States on Magnetic Ordering in $La_2Ni_{1-x}Mn_{1+x}O_6$. *Phys. Status Solidi B* **2019,** *256* (11), 1900019.
43. Zhao, S.; Shi, L.; Zhou, S.; Zhao, J.; Yang, H.; Guo, Y., Size-dependent magnetic properties and Raman spectra of La_2NiMnO_6 nanoparticles. *J. Appl. Phys.* **2009,** *106* (12), 123901/1-123901/5.
44. Chakraborty, D.; Nandi, U.; Dey, A. K.; Dasgupta, P.; Poddar, A.; Jana, D., Effect of Annealing Temperature on the Structural and the Electrical Transport Properties of La_2NiMnO_6 Nanoparticles. *Phys. Status Solidi B* **2018,** *255* (4), 1700436.
45. Pavitra, E.; Raju, G. S. R.; Ghoreishian, S. M.; Kwak, C. H.; Park, J. Y.; Han, Y.-K.; Huh, Y. S., Novel orange-emitting $Ba_2LaNbO_6:Eu^{3+}$ nanophosphors for NUV-based WLEDs and photocatalytic water purification. *Ceram. Int.* **2019,** *45* (4), 4781-4789.
46. Mao, Y.; Parsons, J.; McCloy, J. S., Magnetic properties of double perovskite La_2BMnO_6 (B = Ni or Co) nanoparticles. *Nanoscale* **2013,** *5* (11), 4720-4728.
47. Mao, Y., Facile molten-salt synthesis of double perovskite La_2BMnO_6 nanoparticles. *RSC Adv.* **2012,** *2* (33), 12675-12678.

48. Maiti, R. P.; Dutta, S.; Mitra, M. K.; Chakravorty, D., Large magnetodielectric effect in nanocrystalline double perovskite Y_2FeCrO_6. *J. Phys. D: Appl. Phys.* **2013,** *46* (41), 415303.
49. Alam, M.; Karmakar, K.; Pal, M.; Mandal, K., Electrochemical supercapacitor based on double perovskite Y_2NiMnO_6 nanowires. *RSC Adv.* **2016,** *6* (115), 114722-114726.
50. Kim, J.; Chen, X.; Shih, P.-C.; Yang, H., Porous Perovskite-Type Lanthanum Cobaltite as Electrocatalysts toward Oxygen Evolution Reaction. *ACS Sustain. Chem. Eng.* **2017,** *5* (11), 10910-10917.
51. Zhang, J.; Zhao, Y.; Zhao, X.; Liu, Z.; Chen, W., Porous Perovskite $LaNiO_3$ Nanocubes as Cathode Catalysts for Li-O_2 Batteries with Low Charge Potential. *Sci. Rep.* **2014,** *4*, 6005.
52. Wang, X.; Cao, W.; Qin, L.; Lin, T.; Chen, W.; Lin, S.; Yao, J.; Zhao, X.; Zhou, M.; Hang, C.; Wei, H., Boosting the peroxidase-like activity of nanostructured nickel by inducing its 3+ oxidation state in $LaNiO_3$ perovskite and its application for biomedical assays. *Theranostics* **2017,** *7* (8), 2277-2286.
53. Peng, C.; Rao, C.; Ji, Y.; Zhang, L.; Liu, W.; Wang, X.; Xu, X.; Wang, Z.; Zhang, N.; Peng, H., Double-shelled hollow $LaNiO_3$ nanocage as nanoreactors with remarkable catalytic performance: Illustrating the special morphology and performance relationship. *Molecular Catalysis* **2018,** *455*, 57-67.
54. Dass, R. I.; Yan, J. Q.; Goodenough, J. B., Oxygen stoichiometry, ferromagnetism, and transport properties of $La_{2-x}NiMnO_{6+\delta}$. *Phys. Rev. B: Condens. Matter Mater. Phys.* **2003,** *68* (6), 064415.
55. Liu, Y.; Dai, H.; Deng, J.; Zhang, L.; Zhao, Z.; Li, X.; Wang, Y.; Xie, S.; Yang, H.; Guo, G., Controlled Generation of Uniform Spherical $LaMnO_3$, $LaCoO_3$, Mn_2O_3, and Co_3O_4 Nanoparticles and Their High Catalytic Performance for Carbon Monoxide and Toluene Oxidation. *Inorg. Chem.* **2013,** *52* (15), 8665-8676.
56. McBean, C. L.; Liu, H.; Scofield, M. E.; Li, L.; Wang, L.; Bernstein, A.; Wong, S. S., Generalizable, Electroless, Template-Assisted Synthesis and Electrocatalytic Mechanistic Understanding of Perovskite $LaNiO_3$ Nanorods as Viable, Supportless Oxygen Evolution Reaction Catalysts in Alkaline Media. *ACS Appl. Mater. Interfaces* **2017,** *9* (29), 24634-24648.
57. Jadhav, S. V.; Nikam, D. S.; Khot, V. M.; Thorat, N. D.; Phadatare, M. R.; Ningthoujam, R. S.; Salunkhe, A. B.; Pawar, S. H., Studies on colloidal stability of poly(vinylpyrrolidone)-coated LSMO nanoparticles for magnetic fluid hyperthermia. *New J. Chem.* **2013,** *37* (10), 3121-3130.
58. Koczkur, K. M.; Mourdikoudis, S.; Polavarapu, L.; Skrabalak, S. E., Polyvinylpyrrolidone (PVP) in nanoparticle synthesis. *Dalton Trans.* **2015,** *44* (41), 17883-17905.
59. Casale, A.; De Robertis, A.; De Stefano, C.; Gianguzza, A.; Patane, G.; Rigano, C.; Sammartano, S., Thermodynamic parameters for the formation of glycine complexes with magnesium(II), calcium(II), lead(II), manganese(II), cobalt(II), nickel(II), zinc(II) and cadmium(II) at different temperatures and ionic strengths, with particular reference to natural fluid conditions. *Thermochim. Acta* **1995,** *255*, 109-141.
60. Komova, O. V.; Mukha, S. A.; Ozerova, A. M.; Odegova, G. V.; Simagina, V. I.; Bulavchenko, O. A.; Ishchenko, A. V.; Netskina, O. V., The Formation of Perovskite during the Combustion of an Energy-Rich Glycine–Nitrate Precursor. *Materials* **2020,** *13* (22), 5091.
61. Hammami, R.; Batis, H., Combustion synthesized crystalline La-Mn perovskite catalysts: Role of fuel molecule on thermal and chemical events. *Arab. J. Chem.* **2020,** *13* (1), 683-693.

62. Uekawa, N.; Yamashita, R.; Jun Wu, Y.; Kakegawa, K., Effect of alkali metal hydroxide on formation processes of zinc oxide crystallites from aqueous solutions containing $Zn(OH)_4^{2-}$ ions. *Phys. Chem. Chem. Phys.* **2004,** *6* (2), 442-446.
63. Hojamberdiev, M.; Xu, Y.; Wang, F.; Wang, J.; Liu, W.; Wang, M., Morphology-controlled hydrothermal synthesis of bismuth ferrite using various alkaline minralizers. *Ceramics – Silikáty* **2009,** *53*, 113-117.
64. Ogugua, S. N.; Swart, H. C.; Ntwaeaborwa, O. M., The influence of post-preparation annealing atmospheres on the optical properties and energy transfer between Pr^{3+} and Dy^{3+} in mixed lanthanum-yttrium oxyorthosilicate hosts. *Opt. Mater.* **2018,** *76*, 125-140.
65. Mullica, D. F.; Lok, C. K. C.; Perkins, H. O.; Young, V., X-ray photoelectron final-state screening in $La(OH)_3$: A multiplet structural analysis. *Phys. Rev. B* **1985,** *31* (6), 4039-4042.
66. Mickevicius, S.; Grebinskij, S.; Bondarenka, V.; Vengalis, B.; Sliuziene, K.; Orlowski, B. A.; Osinniy, V.; Drube, W., Investigation of epitaxial LaNiO3-x thin films by high-energy XPS. *J. Alloys Compd.* **2006,** *423* (1-2), 107-111.
67. Li, J. P. H.; Zhou, X.; Pang, Y.; Zhu, L.; Vovk, E. I.; Cong, L.; van Bavel, A. P.; Li, S.; Yang, Y., Understanding of binding energy calibration in XPS of lanthanum oxide by in situ treatment. *Phys. Chem. Chem. Phys.* **2019,** *21* (40), 22351-22358.
68. Moulder, J. F.; Chastain, J., *Handbook of X-ray Photoelectron Spectroscopy*. Physical Electronics Division, Perkin-Elmer Corporation: 1992.
69. Yang, X.; Xue, J.; Feng, L., Pt nanoparticles anchored over Te nanorods as a novel and promising catalyst for methanol oxidation reaction. *Chem. Commun.* **2019,** *55* (75), 11247-11250.
70. Teng, X.; Shan, A.; Zhu, Y.; Wang, R.; Lau, W.-M., Promoting methanol-oxidation-reaction by loading PtNi nano-catalysts on natural graphitic-nano-carbon. *Electrochim. Acta* **2020,** *353*, 136542.
71. Dubouis, N.; Grimaud, A., The hydrogen evolution reaction: from material to interfacial descriptors. *Chem. Sci.* **2019,** *10* (40), 9165-9181.
72. Bull, C. L.; Gleeson, D.; Knight, K. S., Determination of B-site ordering and structural transformations in the mixed transition metal perovskites La_2CoMnO_6 and La_2NiMnO_6. *J. Phys. Condens. Matter* **2003,** *15* (29), 4927-4936.

Figure Captions

Figure 1. XRD patterns of as-prepared LNMO NRs, LNMO NCs, LNO NCs, and LMO NCs, along with the LNMO reference pattern.[72]

Figure 2. Representative (A, E, I) SEM images, (B, F, J) TEM images, (C, G, K) HRTEM images with measured *d*-spacings, and (D, H, L) selected area electron diffraction data for (A-D) LMO NCs, (E-H) LNO NCs, and (I-L) LNMO-8.9 NCs, respectively.

Figure 3. Representative (A, E, I) SEM images, (B, F, J) TEM images, (C, G, K) HRTEM images with measured *d*-spacings, and (D, H, L) selected area electron diffraction data for (A-D) LNMO-8.7 NCs, (E-H) LNMO-9.3 NCs, and (I-L) LNMO NRs, respectively.

Figure 4. EDS mapping data for (A) LNMO-8.9 NCs, (B) LMO NCs, (C) LNO NCs, and (D) LNMO NRs, respectively.

Figure 5. (A) XRD patterns. (B) Plot summarizing the effect of pH on size. (C-J) SEM images of LNMO NCs synthesized with a pH of (C) 8.2, (D) 8.4, (E) 8.7, (F) 8.8, (G) 8.9, (H) 9.0, (I) 9.1, and (J) 9.3, respectively.

Figure 6. Pt 4*d* XPS spectra corresponding to LNO/Pt, LMO/Pt, LNMO-8.9/Pt, LNMO-8.7/Pt, LNMO-9.3/Pt, and LNMO NRs/Pt, respectively. The dashed black line located at 315 eV indicates the expected position for bulk Pt^0.

Figure 7. Representative CV curves of various types of systems tested associated with different perovskite metal oxide chemical compositions. Data were collected in an Ar-saturated 0.1 M $HClO_4$ solution for LNO/Pt, LMO/Pt, LNMO-8.7/Pt, LNMO-8.9/Pt, LNMO-9.3/Pt, LNMO NRs/Pt and Pt/C, respectively.

Figure 8. Probing the Effect of Chemical Composition, Size, and Morphology. MOR activity of La-based perovskite NCs with average sizes of ~200 nm, used as Pt supports within an Ar-

saturated 0.1 M $HClO_4$ + 0.5 M MeOH solution. (A, C) LSV curves compare the effects of varying composition, size, and morphology, respectively. (B, D) The corresponding bar graphs depict the MOR activity observed at 0.8 V.

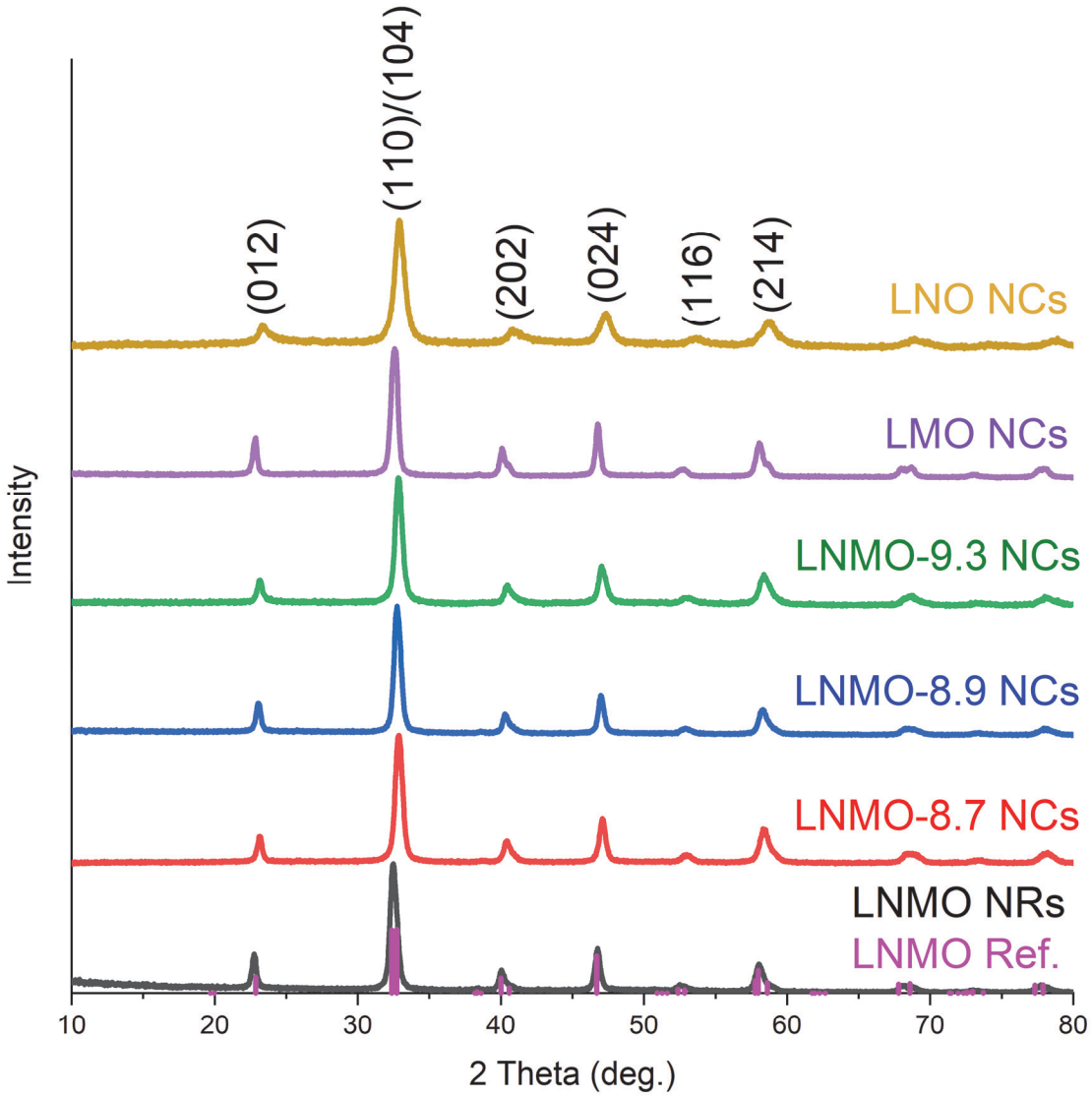
(012)
(110)/(104)
(202)
(024)
(116)
(214)
LNO NCs
LMO NCs
LNMO-9.3 NCs
LNMO-8.9 NCs
LNMO-8.7 NCs
LNMO NRs
LNMO Ref.
Intensity
10
20
30
40
50
60
70
80
2 Theta (deg.)

Figure 1.

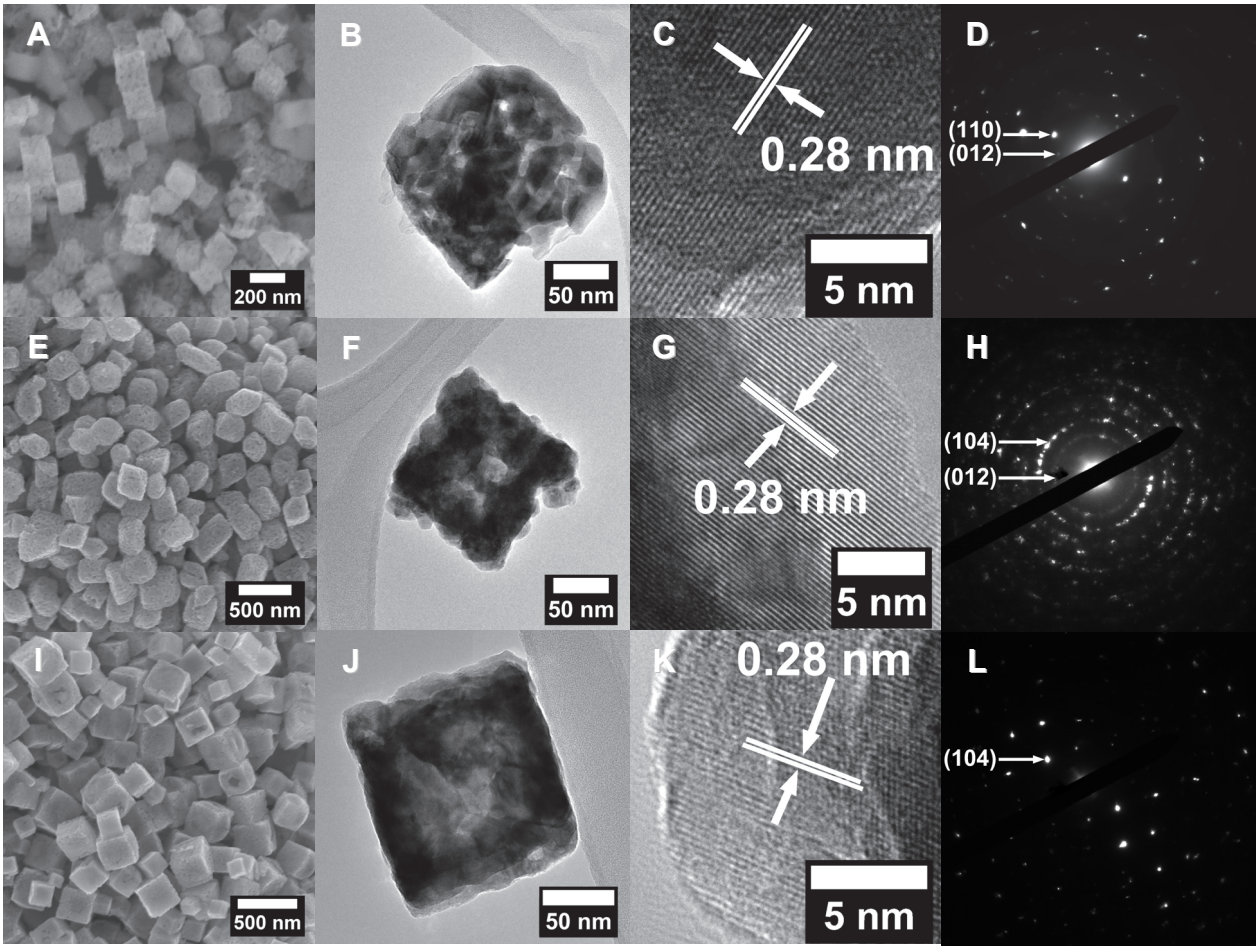
A
200 nm
B
50 nm
C
0.28 nm
5 nm
D
(110)
(012)
E
500 nm
F
50 nm
G
0.28 nm
5 nm
H
(104)
(012)
I
500 nm
J
50 nm
K
0.28 nm
5 nm
L
(104)

Figure 2.

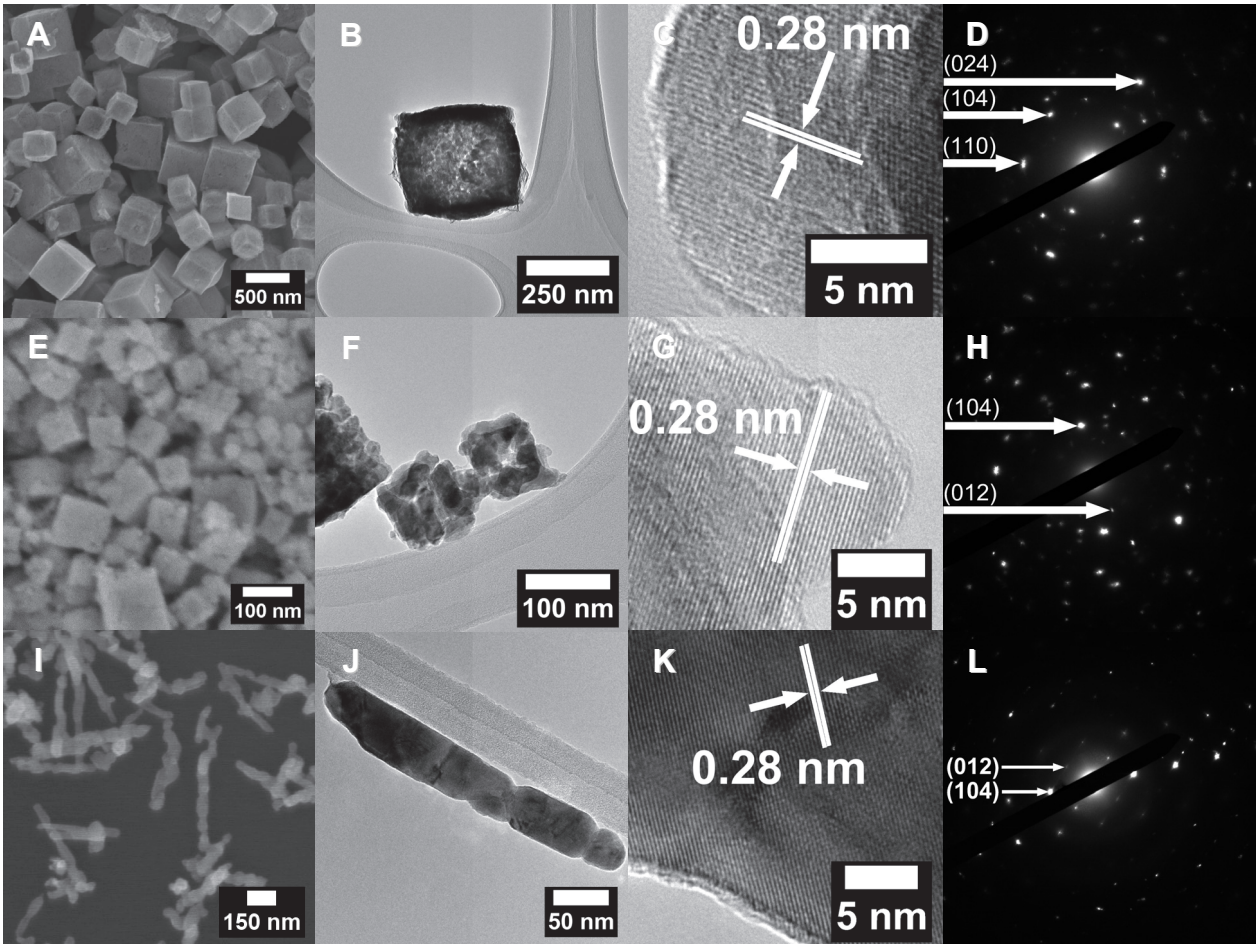
A
500 nm
B
250 nm
C
0.28 nm
5 nm
D
(024)
(104)
(110)
E
100 nm
F
100 nm
G
0.28 nm
5 nm
H
(104)
(012)
I
150 nm
J
50 nm
K
0.28 nm
5 nm
L
(012)
(104)

Figure 3.

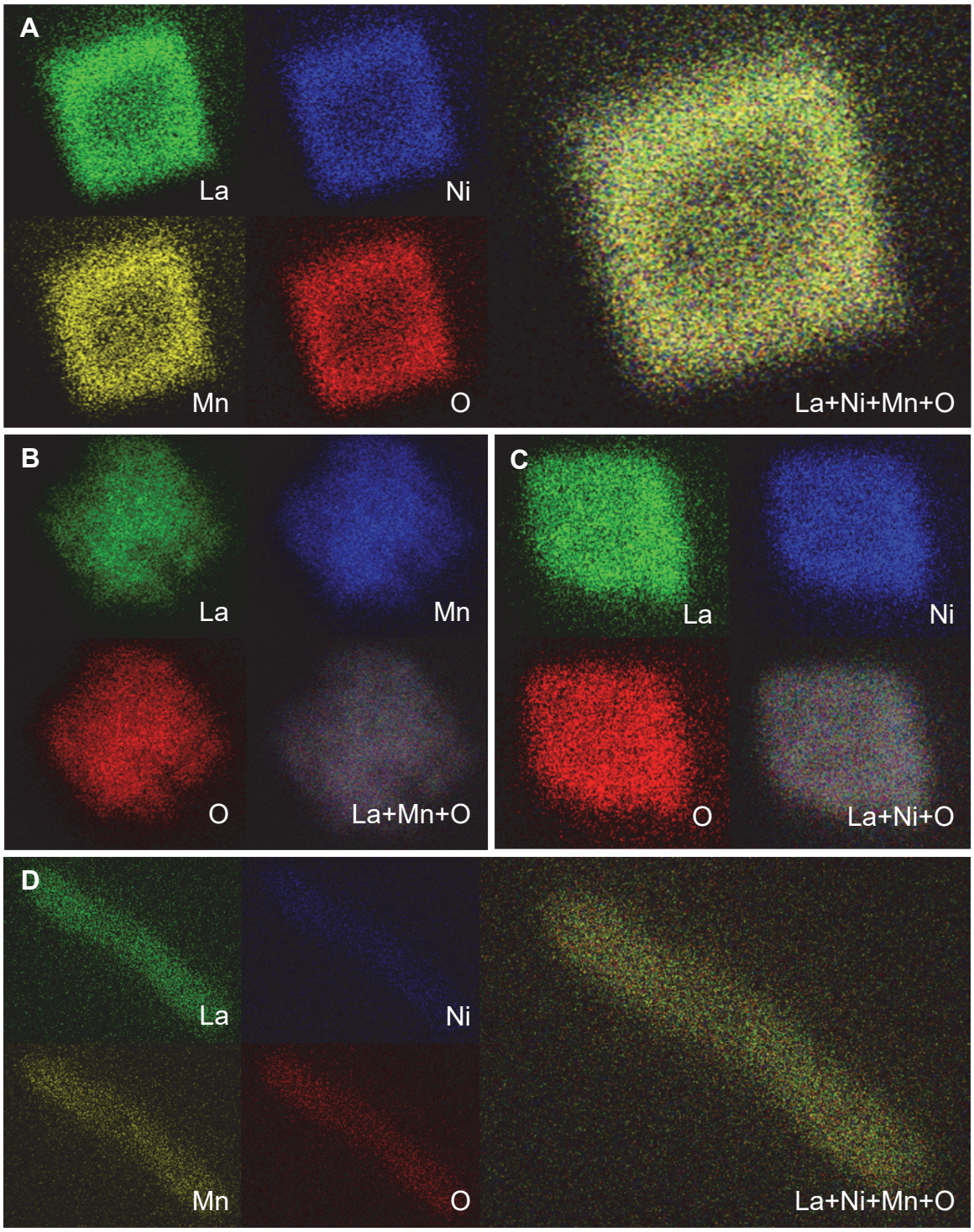
A
La
Ni
Mn
O
La+Ni+Mn+O
B
La
Mn
O
La+Mn+O
C
La
Ni
O
La+Ni+O
D
La
Ni
Mn
O
La+Ni+Mn+O

Figure 4.

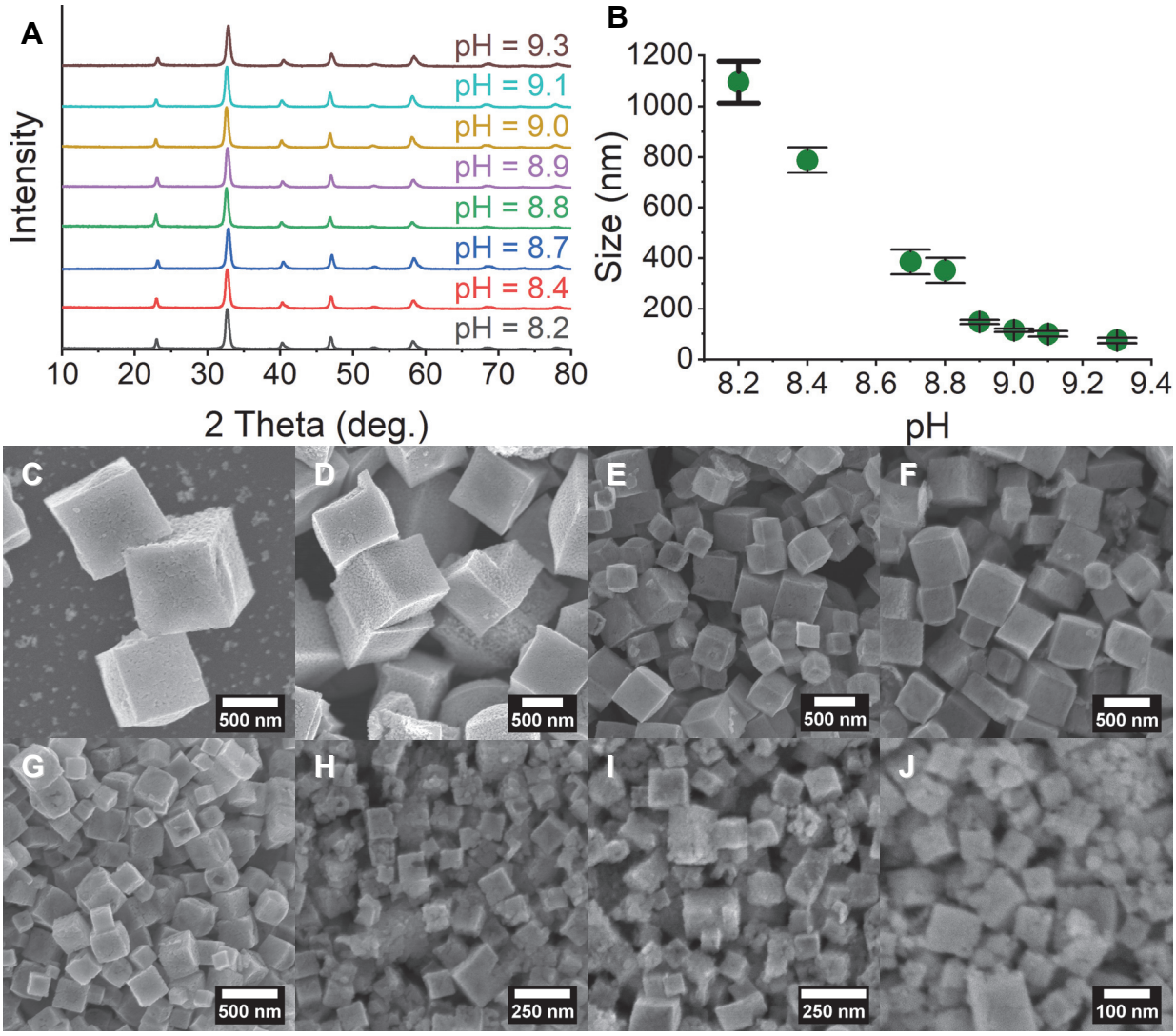
A
Intensity
pH = 9.3
pH = 9.1
pH = 9.0
pH = 8.9
pH = 8.8
pH = 8.7
pH = 8.4
pH = 8.2
10 20 30 40 50 60 70 80
2 Theta (deg.)
B
Size (nm)
1200
1000
800
600
400
200
0
8.2 8.4 8.6 8.8 9.0 9.2 9.4
pH
C
D
E
F
G
H
I
J
500 nm
500 nm
500 nm
500 nm
500 nm
250 nm
250 nm
100 nm

Figure 5.

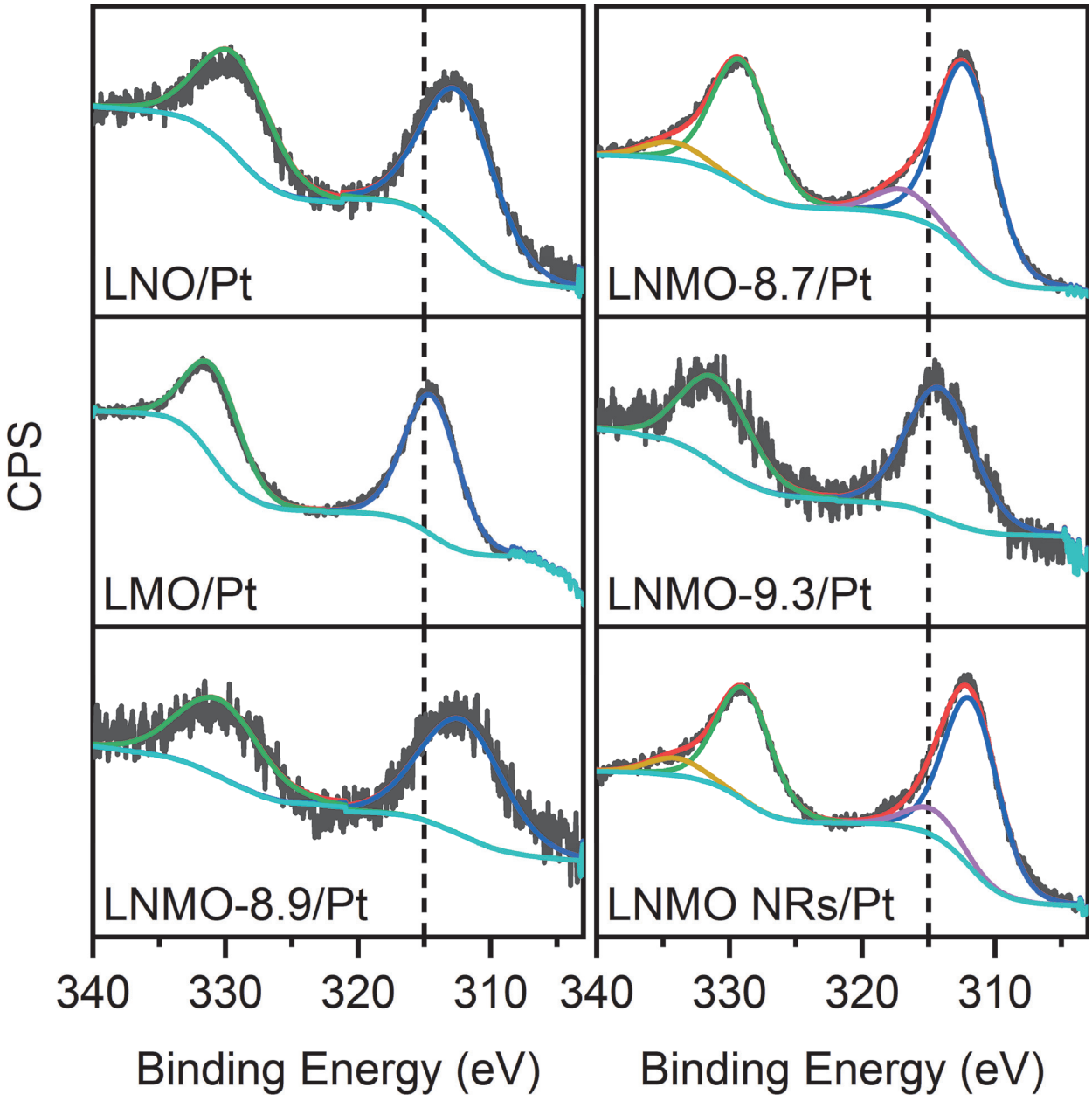
LNO/Pt
LNMO-8.7/Pt
LMO/Pt
LNMO-9.3/Pt
LNMO-8.9/Pt
LNMO NRs/Pt
CPS
340
330
320
310
340
330
320
310
Binding Energy (eV)
Binding Energy (eV)

Figure 6.

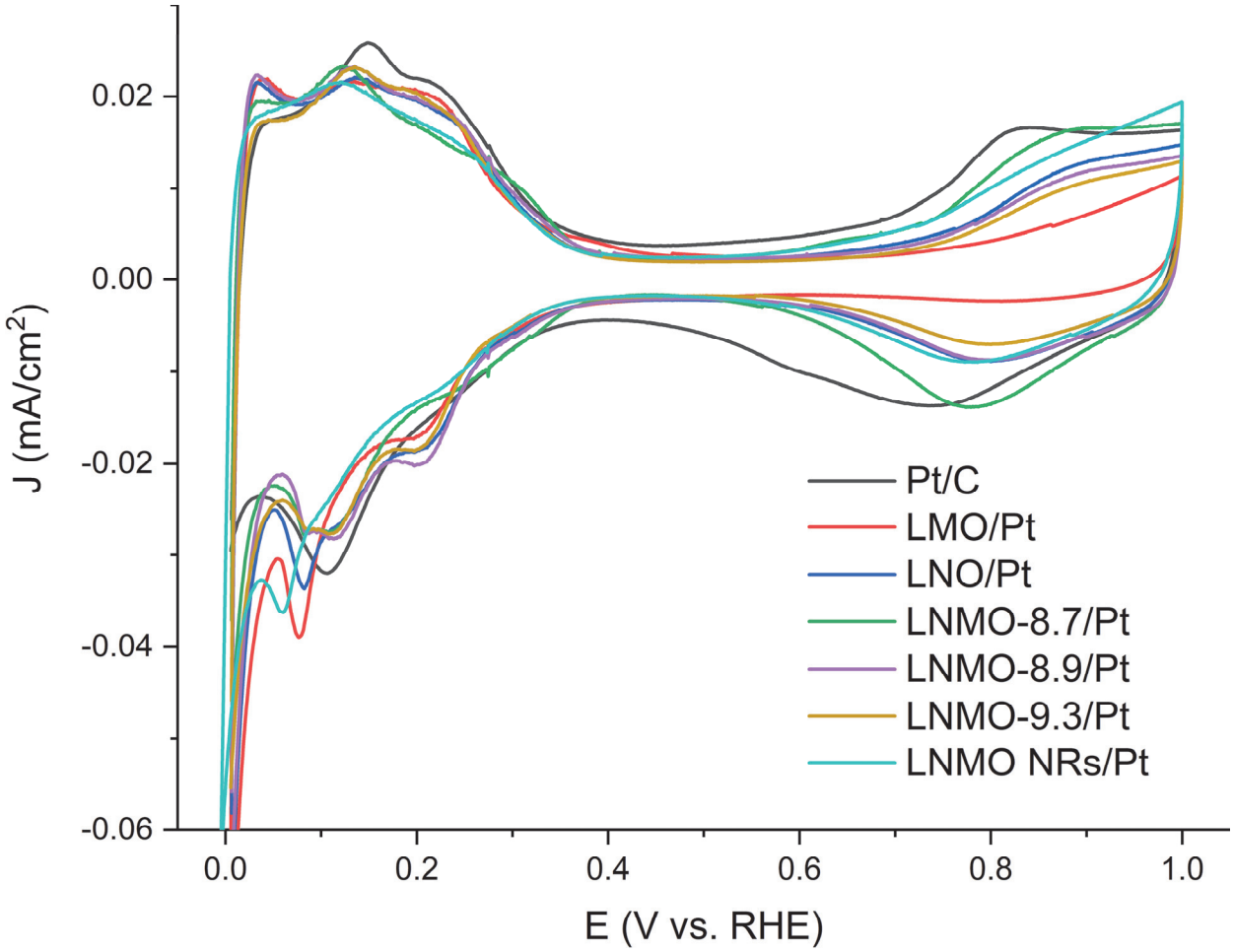
0.02
0.00
-0.02
-0.04
-0.06
J (mA/cm^2)
0.0
0.2
0.4
0.6
0.8
1.0
E (V vs. RHE)
Pt/C
LMO/Pt
LNO/Pt
LNMO-8.7/Pt
LNMO-8.9/Pt
LNMO-9.3/Pt
LNMO NRs/Pt

Figure 7.

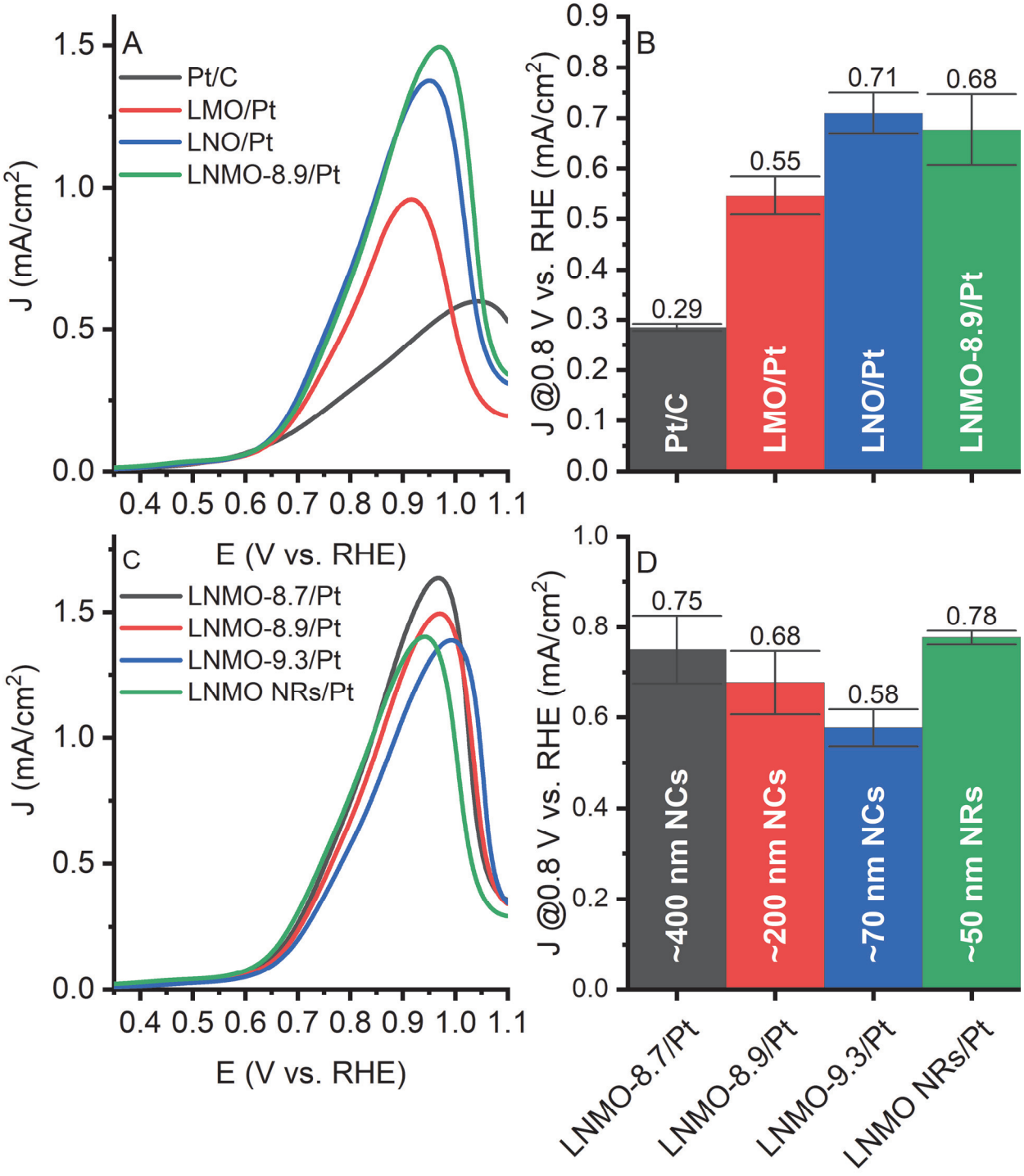
A
Pt/C
LMO/Pt
LNO/Pt
LNMO-8.9/Pt
J (mA/cm^2)
E (V vs. RHE)
B
J @0.8 V vs. RHE (mA/cm^2)
0.29
0.55
0.71
0.68
Pt/C
LMO/Pt
LNO/Pt
LNMO-8.9/Pt
C
LNMO-8.7/Pt
LNMO-8.9/Pt
LNMO-9.3/Pt
LNMO NRs/Pt
D
0.75
0.68
0.58
0.78
~400 nm NCs
~200 nm NCs
~70 nm NCs
~50 nm NRs
LNMO-8.7/Pt
LNMO-8.9/Pt
LNMO-9.3/Pt
LNMO NRs/Pt

Figure 8.

Table 1. Average particle sizes and measured BET surface areas of various, as-prepared perovskite nanostructures.

Sample	**Size (nm)**	**BET surface area (m^2/g)**
LNMO-8.7 NCs	430 ± 113	18.9
LNMO-8.9 NCs	181 ± 50	23.2
LNMO-9.3 NCs	76 ± 21	112.5
LMO NCs	191 ± 41	25.4
LNO NCs	245 ± 60	28.2
LNMO NRs	43 ± 8	108.2

TOC Figure

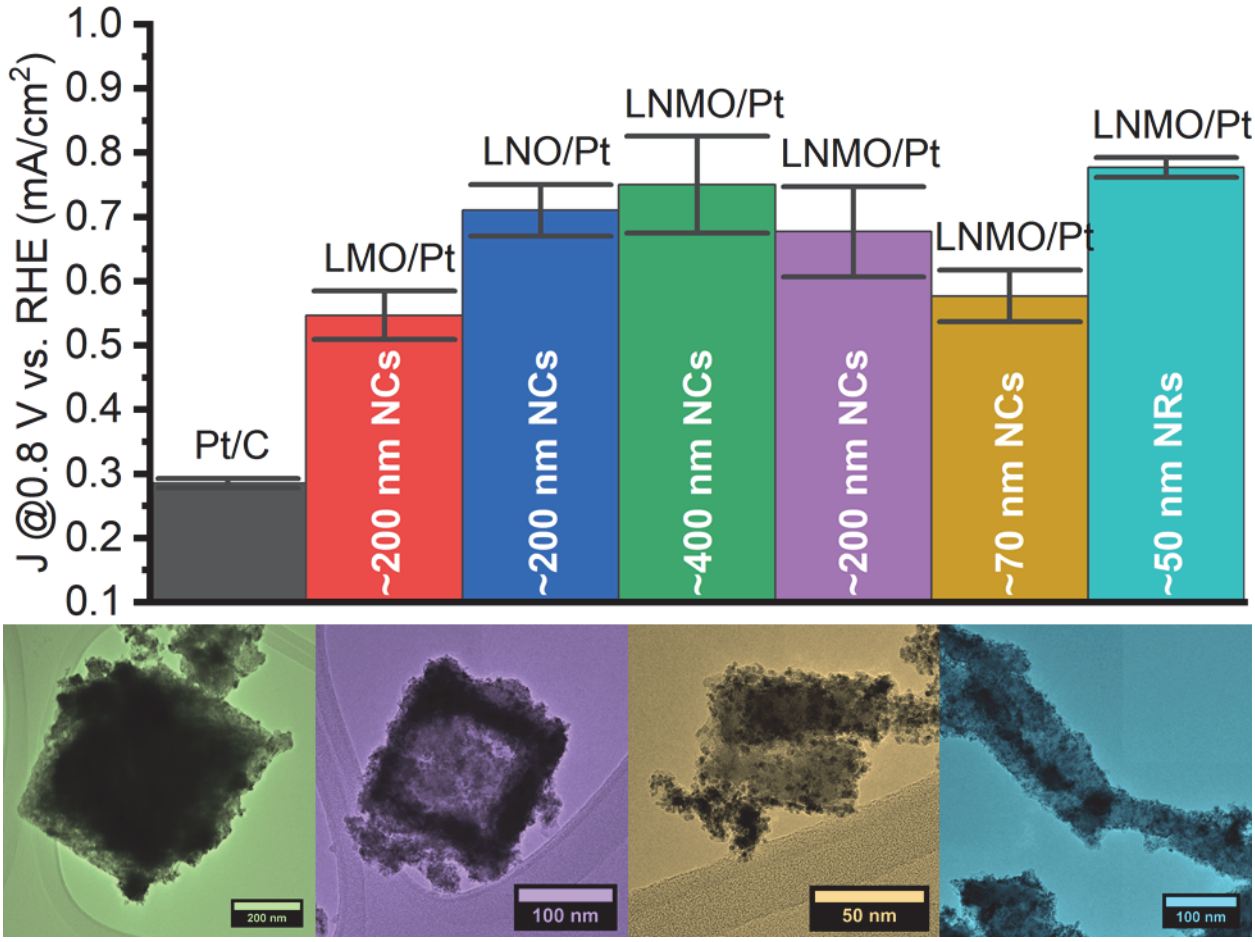
J @0.8 V vs. RHE (mA/cm^2)
1.0
0.9
0.8
0.7
0.6
0.5
0.4
0.3
0.2
0.1
Pt/C
LMO/Pt
~200 nm NCs
LNO/Pt
~200 nm NCs
LNMO/Pt
~400 nm NCs
LNMO/Pt
~200 nm NCs
LNMO/Pt
~70 nm NCs
LNMO/Pt
~50 nm NRs
200 nm
100 nm
50 nm
100 nm